Hindawi
Advances in High Energy Physics
Volume 2022, Article ID 5949610, 20 pages
https://doi.org/10.1155/2022/5949610

Research Article

Random Statistical Analysis of Transverse Momentum Spectra of Strange Particles and Dependence of Related Parameters on Centrality in High Energy Collisions at the LHC

Xu-Hong Zhang,[1] Fu-Hu Liu,[1] Khusniddin K. Olimov,[2,3] and Airton Deppman[4]

[1]*Institute of Theoretical Physics, State Key Laboratory of Quantum Optics and Quantum Optics Devices & Collaborative Innovation Center of Extreme Optics, Shanxi University, Taiyuan 030006, China*
[2]*Physical-Technical Institute of Uzbekistan Academy of Sciences, Chingiz Aytmatov Str. 2b, 100084 Tashkent, Uzbekistan*
[3]*National University of Science and Technology MISIS (NUST MISIS), Almalyk branch, Almalyk, Uzbekistan*
[4]*Instituto de Física, Universidade de São Paulo, Rua do Matão 1371-Butantã, São Paulo CEP 05580-090, Brazil*

Correspondence should be addressed to Fu-Hu Liu; fuhuliu@163.com

Received 12 May 2022; Revised 9 September 2022; Accepted 10 October 2022; Published 2 November 2022

Academic Editor: Edward Sarkisyan Grinbaum

We have studied the transverse momentum (p_T) spectra of the final-state strange particles, including $K^{\pm}$, ϕ, Ξ, and Ω, produced in high energy lead–lead (Pb–Pb), proton–lead (p–Pb), xenon–xenon (Xe–Xe) collisions at the Large Hadron Collider (LHC). Taking into account the contribution of multiquark composition, whose probability density distribution is described by the modified Tsallis–Pareto-type function; we simulate the p_T spectra of the final-state strange particles by a Monte Carlo method, which is shown to be in good agreement with the experimental data in most the cases. The kinetic freeze-out parameters are obtained. The present method provides a new tool for studying the spectra of various particles produced in high energy collisions, reflecting more realistically the collision process, which is of great significance to study the formation and properties of the produced particles.

1. Introduction

Plenty of final-state particles are produced in relativistic heavy-ion collisions [1, 2] in various collision processes, resulting in different configurations of final-state particles. In high energy collisions, novel physical phenomena can appear with the most representative being formation of quark-gluon plasma (QGP) [3, 4]. In addition, multiparticle production provides abundant information on thermal and statistical properties of a system. Although quantum chromodynamics (QCD) can provide an important theoretical basis to study strong interactions among quarks and features of collision system [5, 6], thermal and statistical method is still a powerful tool for such analysis.

Investigation of the transverse momentum (p_T) (or transverse mass, m_T) spectra of the final-state particles is an effective and fast method [1, 2] to study the processes of multiparticle production and system evolution. This method can help to obtain the thermodynamic parameters of the final-state particles and collision system. The p_T spectra of different final-state particles have been studied extensively. In addition to baryons, leptons, and other elementary particles have also attracted much attention.

In recent years, the production of single and multistrange particles [7–10] has attracted an increased interest, being extensively researched. Based on the exotic properties [11], the p_T spectra of strange particles measured in high energy collisions by various collaborations have been analyzed and predicted utilizing Tsallis function [12–17], nonequilibrium chemical or kinetic freeze-out model [8], etc.

Relative to pions, enhanced production of multistrange hadrons [10–21] in high-multiplicity proton–proton collisions has been observed experimentally for the first time, and it is found that the integrated yields of strange particles

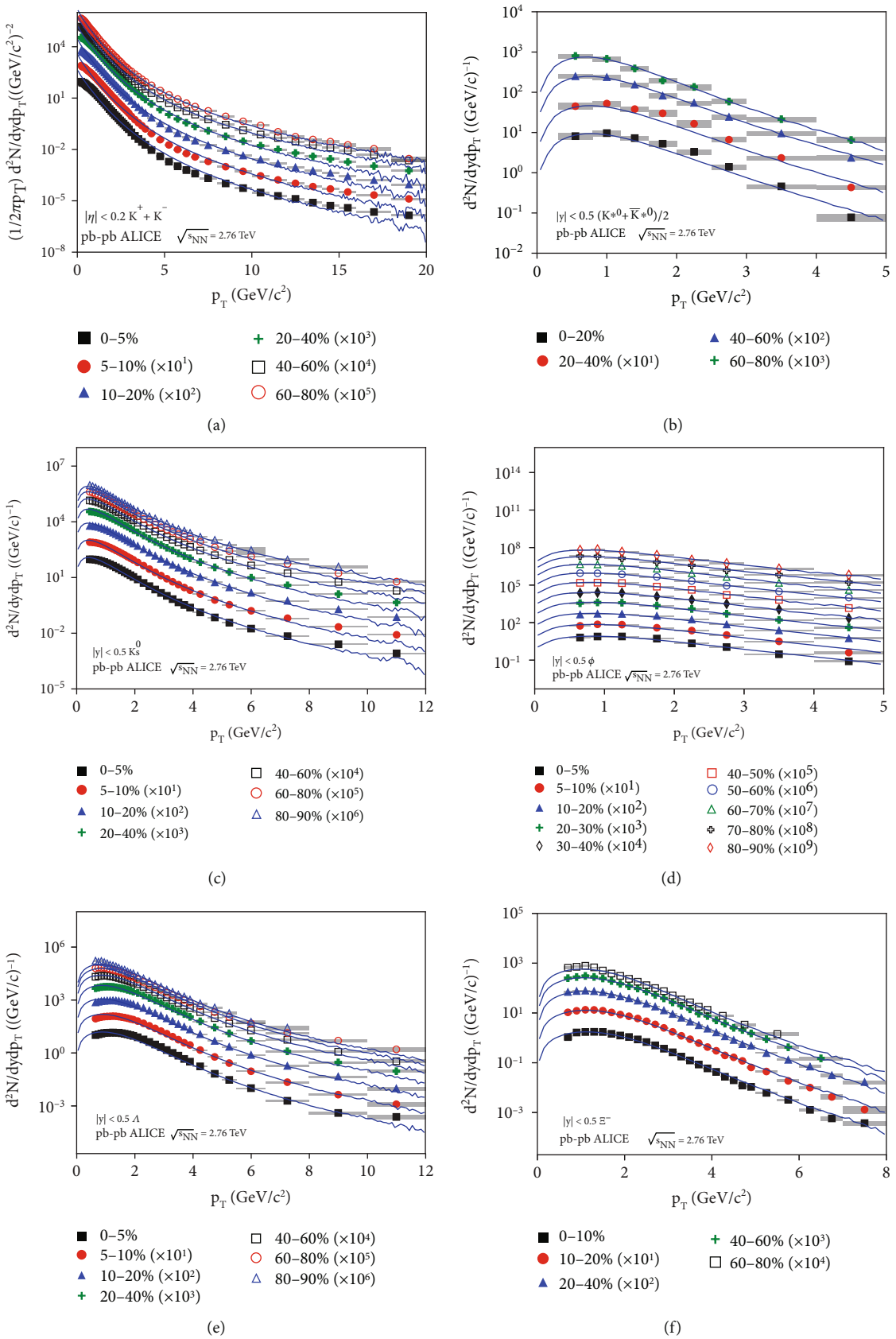

Figure 1: Continued.

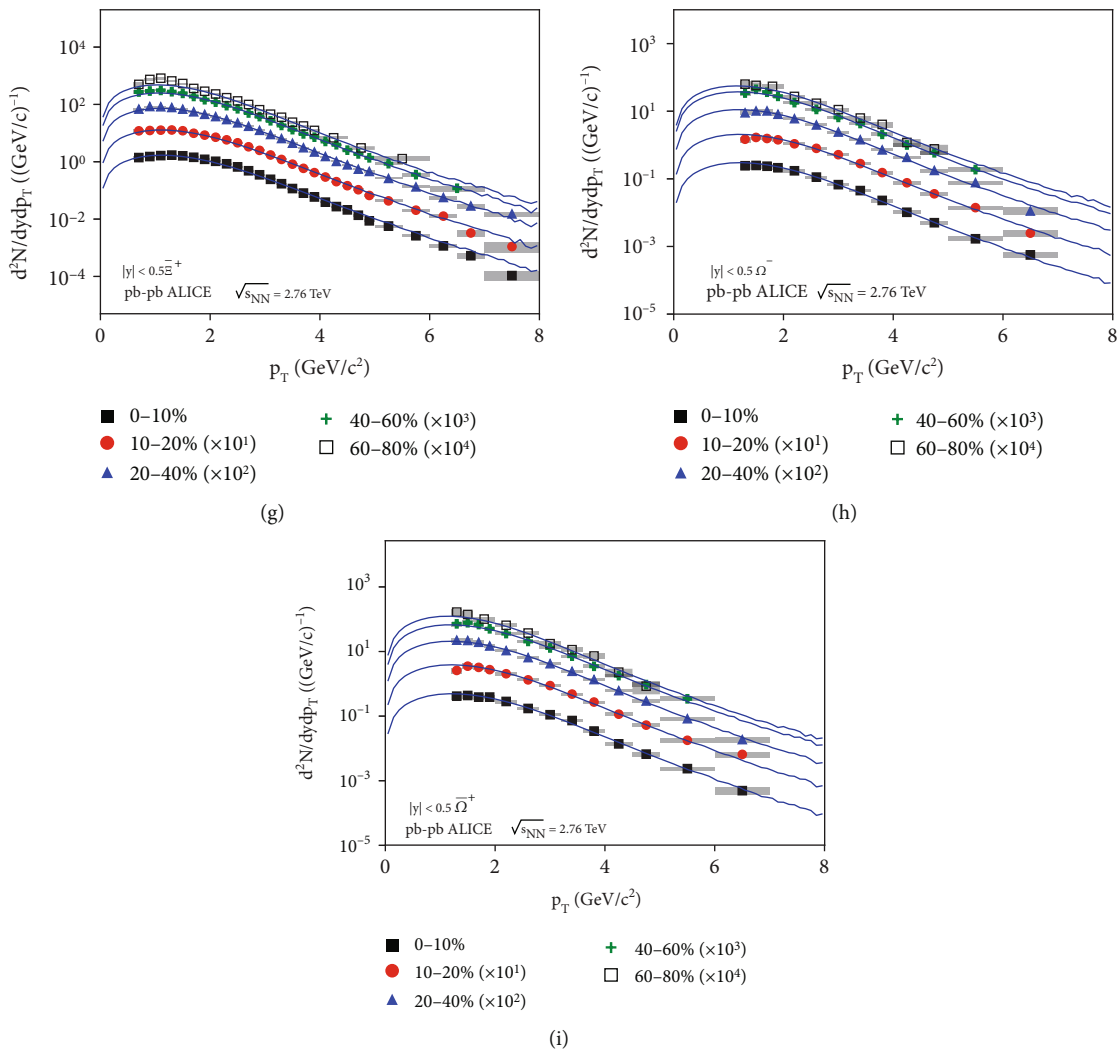

FIGURE 1: The p_T spectra of (a) $K^+ + K^-$, (b) $(K^{*0} + \bar{K}^{*0})/2$, (c) K^0_S, (d) ϕ, (e) Λ, (f) Ξ^-, (g) $\bar{\Xi}^+$, (h) Ω^-, and (i) $\bar{\Omega}^+$ in Pb–Pb collisions with different centrality and mid-pseudorapidity intervals at $\sqrt{s_{NN}} = 2.76$ TeV. The symbols represent the data measured by the ALICE Collaboration [39–41]. The solid curves represent the Monte Carlo results, based on the probability density function Equation (2) and the p_T expression in Equation (6).

increases significantly with the event charged-particle multiplicity. Besides, the azimuthal angular correlation and the mass dependence of p_T due to the existence of QGP in high-energy collisions have been also reported. Further researches on strange particles can better explore and reveal the properties of QGP.

We are interested in the exploration of the properties of different strange particles. In contrast to our previous work [22–24], in this work we adopt a new algorithm to simulate and analyze the p_T spectra of strange particles. We aim to restore the collision process more realistically and extract more accurate characteristic parameters. The multiquark composition of baryons is considered. A Monte Carlo method [25–27] is used to simulate different transverse momenta carried by various quarks. The modified Tsallis–Pareto-type function [22–24] is used to define the contribution of multiquarks, from which the kinetic freeze-out temperature (T_0) [28–31], average transverse flow velocity ($\langle\beta_t\rangle$) [32, 33], and other related parameters can be directly extracted.

This paper is structured as follows. The formalism and Monte Carlo method are briefly introduced in Section 2. The simulated or fitted results, their comparison with the data, and discussion are given in Section 3. Finally, in Section 4 we summarize our main observations and conclusions.

2. Formalism and Method

To deal with p_T of strange particles produced in high energy collisions, we briefly introduce the analysis, based on the Monte Carlo method. Generally, the modified Tsallis–Pareto-type function [22–24].

$$f(p_T) = \frac{1}{N}\frac{dN}{dp_T} = Cp_T^{a_0}\left(1 + \frac{m_T - m_0}{nT}\right)^{-n}, \quad (1)$$

Table 1: Values of n, T_0, a_0, $\langle\beta_t\rangle$, χ^2, and ndof corresponding to the solid curves in Figure 1.

Figure	Particle	$\sqrt{s_{\mathrm{NN}}}$ (TeV)	Selection	n	T_0 (GeV)	a_0	$\langle\beta_t\rangle$ (c)	χ^2/ndof
Figure 1(a)	$K^+ + K^-$	2.76	0–5%	7.1 ± 0.2	0.221 ± 0.003	-0.022 ± 0.004	0.247 ± 0.005	1199/53
		$\lvert\eta\rvert < 0.2$	5–10%	7.0 ± 0.2	0.219 ± 0.003	-0.024 ± 0.004	0.246 ± 0.005	1021/53
		Pb–Pb	10–20%	6.9 ± 0.2	0.216 ± 0.003	-0.026 ± 0.004	0.244 ± 0.005	887/53
			20–40%	6.7 ± 0.2	0.212 ± 0.003	-0.029 ± 0.004	0.241 ± 0.005	793/53
			40–60%	6.2 ± 0.2	0.209 ± 0.003	-0.032 ± 0.004	0.238 ± 0.005	323/53
			60–80%	6.1 ± 0.2	0.208 ± 0.003	-0.035 ± 0.004	0.234 ± 0.005	115/53
Figure 1(b)	$\left(K^{*0} + \bar{K}^{*0}\right)/2$	2.76	0–20%	7.7 ± 0.2	0.174 ± 0.003	1.042 ± 0.010	0.309 ± 0.006	21/3
		$\lvert y\rvert < 0.5$	20–40%	7.4 ± 0.2	0.170 ± 0.003	1.037 ± 0.010	0.306 ± 0.006	22/3
		Pb–Pb	40–60%	7.2 ± 0.2	0.164 ± 0.003	1.032 ± 0.010	0.301 ± 0.006	3/3
			60–80%	6.9 ± 0.2	0.152 ± 0.003	1.027 ± 0.010	0.294 ± 0.006	3/3
Figure 1(c)	K^0_S	2.76	0–5%	8.1 ± 0.2	0.179 ± 0.003	0.227 ± 0.005	0.310 ± 0.006	357/28
		$\lvert y\rvert < 0.5$	5–10%	8.0 ± 0.2	0.177 ± 0.003	0.226 ± 0.005	0.307 ± 0.006	337/28
		Pb–Pb	10–20%	7.8 ± 0.2	0.175 ± 0.003	0.224 ± 0.005	0.305 ± 0.006	348/28
			20–40%	7.5 ± 0.2	0.174 ± 0.003	0.220 ± 0.005	0.303 ± 0.006	318/28
			40–60%	7.1 ± 0.2	0.171 ± 0.003	0.218 ± 0.005	0.301 ± 0.006	221/28
			60–80%	6.7 ± 0.2	0.169 ± 0.003	0.214 ± 0.005	0.298 ± 0.006	151/28
			80–90%	6.4 ± 0.2	0.168 ± 0.003	0.210 ± 0.005	0.295 ± 0.006	46/28
Figure 1(d)	ϕ	2.76	0–5%	8.6 ± 0.2	0.183 ± 0.003	1.013 ± 0.009	0.311 ± 0.006	14/3
		$\lvert y\rvert < 0.5$	5–10%	8.5 ± 0.2	0.181 ± 0.003	1.012 ± 0.009	0.309 ± 0.006	31/3
		Pb–Pb	10–20%	8.3 ± 0.2	0.179 ± 0.003	1.011 ± 0.009	0.308 ± 0.006	20/3
			20–30%	8.2 ± 0.2	0.176 ± 0.003	1.009 ± 0.009	0.305 ± 0.006	7/3
			30–40%	7.9 ± 0.2	0.174 ± 0.003	1.006 ± 0.009	0.302 ± 0.006	8/3
			40–50%	7.7 ± 0.2	0.171 ± 0.003	0.999 ± 0.009	0.299 ± 0.006	5/3
			50–60%	7.4 ± 0.2	0.166 ± 0.003	0.996 ± 0.009	0.296 ± 0.006	3/3
			60–70%	7.1 ± 0.2	0.162 ± 0.003	0.991 ± 0.009	0.287 ± 0.006	1/3
			70–80%	6.9 ± 0.2	0.158 ± 0.003	0.987 ± 0.009	0.285 ± 0.006	4/3
			80–90%	6.6 ± 0.2	0.154 ± 0.003	0.982 ± 0.009	0.282 ± 0.006	2/3
Figure 1(e)	Λ	2.76	0–5%	10.0 ± 0.2	0.137 ± 0.002	1.429 ± 0.012	0.218 ± 0.004	272/26
		$\lvert y\rvert < 0.5$	5–10%	9.8 ± 0.2	0.135 ± 0.002	1.426 ± 0.012	0.216 ± 0.004	211/26
		Pb–Pb	10–20%	9.7 ± 0.2	0.134 ± 0.002	1.420 ± 0.012	0.213 ± 0.004	197/26
			20–40%	9.5 ± 0.2	0.132 ± 0.002	1.419 ± 0.012	0.212 ± 0.004	127/26
			40–60%	9.2 ± 0.2	0.128 ± 0.002	1.416 ± 0.012	0.210 ± 0.004	32/26
			60–80%	9.0 ± 0.2	0.126 ± 0.002	1.413 ± 0.012	0.207 ± 0.004	38/26
			80–90%	8.8 ± 0.2	0.122 ± 0.002	1.410 ± 0.012	0.204 ± 0.004	60/24
Figure 1(f)	Ξ^-	2.76	0–10%	11.9 ± 0.3	0.137 ± 0.002	1.925 ± 0.014	0.238 ± 0.005	126/22
		$\lvert y\rvert < 0.5$	10–20%	11.8 ± 0.3	0.135 ± 0.002	1.922 ± 0.014	0.236 ± 0.005	63/22
		Pb–Pb	20–40%	11.4 ± 0.2	0.132 ± 0.002	1.918 ± 0.014	0.233 ± 0.005	29/22
			40–60%	10.8 ± 0.2	0.126 ± 0.002	1.912 ± 0.014	0.230 ± 0.005	21/20
			60–80%	10.5 ± 0.2	0.120 ± 0.002	1.904 ± 0.014	0.227 ± 0.005	37/15

Table 1: Continued.

Figure	Particle	$\sqrt{s_{NN}}$ (TeV)	Selection	n	T_0 (GeV)	a_0	$\langle\beta_t\rangle$ (c)	χ^2/ndof
	$\bar{\Xi}^+$	2.76	0–10%	12.1 ± 0.3	0.138 ± 0.002	1.924 ± 0.014	0.235 ± 0.005	122/22
		$\|y\| < 0.5$	10–20%	12.0 ± 0.3	0.136 ± 0.002	1.922 ± 0.014	0.233 ± 0.005	44/22
Figure 1(g)		Pb–Pb	20–40%	11.8 ± 0.3	0.134 ± 0.002	1.918 ± 0.014	0.231 ± 0.005	33/22
			40–60%	11.4 ± 0.3	0.130 ± 0.002	1.911 ± 0.014	0.227 ± 0.005	29/20
			60–80%	11.1 ± 0.2	0.126 ± 0.002	1.910 ± 0.014	0.225 ± 0.005	72/15
	Ω^-	2.76	0–10%	10.7 ± 0.2	0.133 ± 0.002	2.026 ± 0.015	0.248 ± 0.005	5/8
		$\|y\| < 0.5$	10–20%	10.4 ± 0.2	0.131 ± 0.002	2.024 ± 0.015	0.247 ± 0.005	13/8
Figure 1(h)		Pb–Pb	20–40%	10.3 ± 0.2	0.129 ± 0.002	2.022 ± 0.015	0.245 ± 0.005	13/8
			40–60%	10.1 ± 0.2	0.126 ± 0.002	2.020 ± 0.015	0.242 ± 0.005	11/7
			60–80%	9.8 ± 0.2	0.124 ± 0.002	2.018 ± 0.015	0.237 ± 0.005	7/5
	$\bar{\Omega}^+$	2.76	0–10%	10.9 ± 0.2	0.135 ± 0.002	2.022 ± 0.015	0.247 ± 0.005	7/8
		$\|y\| < 0.5$	10–20%	10.8 ± 0.2	0.134 ± 0.002	2.020 ± 0.015	0.245 ± 0.005	13/8
Figure 1(i)		Pb–Pb	20–40%	10.6 ± 0.2	0.132 ± 0.002	2.017 ± 0.015	0.241 ± 0.005	6/8
			40–60%	10.3 ± 0.2	0.130 ± 0.002	2.014 ± 0.015	0.239 ± 0.005	7/7
			60–80%	9.8 ± 0.2	0.122 ± 0.002	2.004 ± 0.015	0.235 ± 0.005	7/5

is suitable to characterize the p_T spectra of final-state particles in low- and intermediate-p_T regions. Here, N is the number of particles; C is the normalization constant; T is the effective temperature of a collision system; n is an entropy-related index, which is used to describe the degree of nonequilibrium of the system; $m_T = \sqrt{p_T^2 + m_0^2}$ is the transverse mass of a particle; m_0 is the rest mass of the particle, and a_0 is the correction index, which makes the function to fit better the spectra in low-p_T region.

It should be noted that when we set $a_0 = 1$. Equation (1) is naturally converged to the Tsallis–Pareto-type function. That is to say, the introduction of $a_0 \neq 1$ in Equation (1) is a modification of Tsallis–Pareto-type function [17]. To extract characteristic parameters such as the thermal or kinetic freeze-out temperature T_0 of a collision system [28–31] and the average transverse flow velocity $\langle\beta_t\rangle$ of the produced particles [32, 33] at the quark level, following References [34–37], we perform the Lorentz-like transformation on m_T and p_T in Equation (1) by using $m_T \longrightarrow \langle\gamma_t\rangle(m_T - p_T\langle\beta_t\rangle)$ and $|p_T| \longrightarrow \langle\gamma_t\rangle|p_T - m_T\langle\beta_t\rangle|$, where $\langle\gamma_t\rangle = 1/\sqrt{1 - \langle\beta_t\rangle^2}$ is the Lorentz factor.

Thus, the transverse momentum p_{Ti} of the i-th quark contributed to the particle p_T is assumed to obey the new modified probability density function

$$f_i(p_{Ti}) = C_i \frac{\langle\gamma_t\rangle^{a_0+1}}{m_{Ti}} (m_{Ti} - p_{Ti}\langle\beta_t\rangle)|p_{Ti} - m_{Ti}\langle\beta_t\rangle|^{a_0} \times \left[1 + \frac{\langle\gamma_t\rangle(m_{Ti} - p_{Ti}\langle\beta_t\rangle) - m_{0i}}{nT_0}\right]^{-n}. \quad (2)$$

The temperature parameter at this time has been naturally converted from T in Equation (1) to the kinetic freeze-out temperature T_0. In Equation (2), m_{0i} is the constituent mass of the i-th quark. As shown in the literature [38], we have $m_{01} = 0.31\text{GeV}/c^2$ for up and down quarks and $m_{02} = 0.5$ GeV/c^2 for a strange quark. Thus, we have constructed the probability density function, which satisfies multiquark states.

Within the defined interval $[0, \infty)$ of p_{Ti} of the i-th quark, we have the normalization condition

$$\int_0^\infty f_i(p_{Ti}) dp_{Ti} = 1, \quad (3)$$

where the upper limit is usually quite a large value, but not infinite. In a Monte Carlo calculation, R_i denotes the random number in [0, 1], and we have the relation satisfied by p_{Ti} to be

$$\int_0^{p_{Ti}} f_i\left(p'_{Ti}\right) dp'_{Ti} < R_i < \int_0^{p_{Ti}+\delta_{p_{Ti}}} f_i\left(p'_{Ti}\right) dp'_{Ti}, \quad (4)$$

where $\delta_{p_{Ti}}$ is a small shift from p_{Ti}. According to Equation (4), one can obtain a series of discrete values of p_{Ti} which satisfy Equation (2). In the calculation, we take $\delta_{p_{Ti}} = 0.01$ GeV/c. Considering the contributions of multiquarks, we have $i = 1$ to 2 for mesons, and $i = 1$ to 3 for baryons, because meson consists of two quarks, and baryon has three quarks.

In general condition, the particle transverse momentum $\boldsymbol{p}_T$ is the vector superposition of $\boldsymbol{p}_{Ti}$ of two or three quarks. In the right-handed Cartesian coordinate system O-xyz, let the Oz axis be the beam direction, xOz plane be the reaction plane, and xOy plane be the transverse one. In the source rest frame, $\boldsymbol{p}_{Ti}$ is assumed to be isotropic. The movement of the source along the Oz axis constitutes the longitudinal flow, and the interactions among different sources causes the transverse

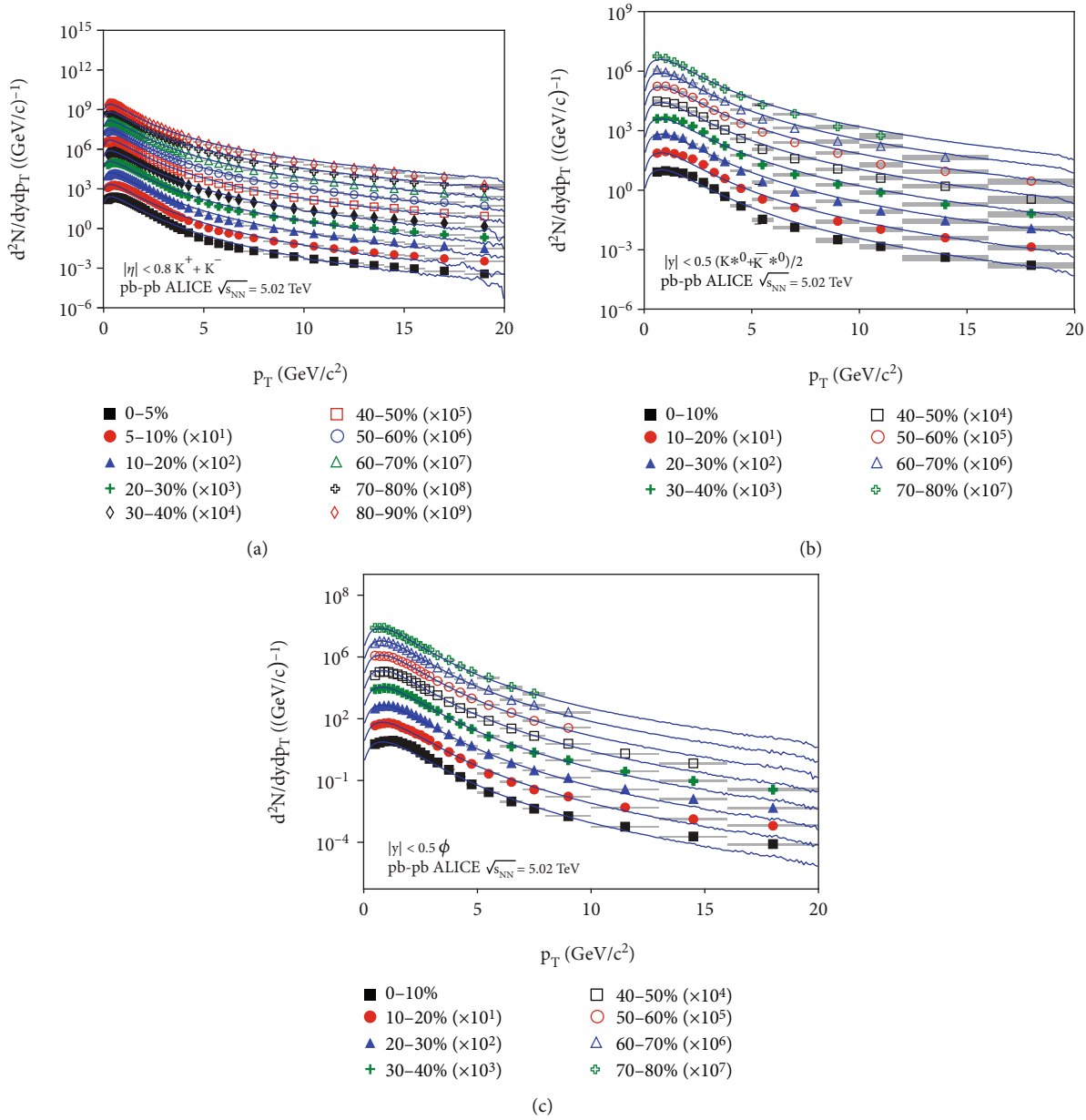

FIGURE 2: The p_T spectra of (a) $K^+ + K^-$, (b) $(K^{*0} + \bar{K}^{*0})/2$, and (c) ϕ in Pb–Pb collisions at $\sqrt{s_{\mathrm{NN}}} = 5.02$ TeV. The symbols represent the data measured by the ALICE Collaboration [42, 43]. The solid curves represent the Monte Carlo results, based on the probability density function Equation (2) and the p_T expression in Equation (6).

flow. The longitudinal flow is not the focus of the present work, though it can be described by the rapidity distribution. The transverse flow is described by the average transverse flow velocity $\langle \beta_t \rangle$ that is mentioned in the above discussion.

For the i-th quark, we have the x- and y-components of $\boldsymbol{p}_{Ti}$ to be

$$\begin{aligned} p_{Tix} &= p_{Ti} \cos \varphi_i = p_{Ti} \cos (2\pi r_i), \\ p_{Tiy} &= p_{Ti} \sin \varphi_i = p_{Ti} \sin (2\pi r_i), \end{aligned} \tag{5}$$

where the isotropic azimuthal angle φ_i is distributed uniformly in $[0, 2\pi]$. Using a random number r_i distributed uniformly in $[0, 1]$, one has $\varphi_i = 2\pi r_i$ in the Monte Carlo calculation. According to the principle of vector superposition, we obtain the expressions of $\boldsymbol{p}_T$'s components and p_T of the final-state particle to be

$$\begin{aligned} p_{Tx} &= \sum_{i=1}^{2,3} p_{Ti} \cos (2\pi r_i), \\ p_{Ty} &= \sum_{i=1}^{2,3} p_{Ti} \sin (2\pi r_i), \\ p_T &= \sqrt{p_{Tx}^2 + p_{Ty}^2}, \end{aligned} \tag{6}$$

Table 2: Values of n, T_0, a_0, $\langle\beta_t\rangle$, χ^2, and ndof corresponding to the solid curves in Figure 2.

Figure	Particle	$\sqrt{s_{NN}}$ (TeV)	Selection	n	T_0 (GeV)	a_0	$\langle\beta_t\rangle$ (c)	χ^2/ndof
Figure 2(a)	$K^+ + K^-$	5.02	0–5%	6.8 ± 0.2	0.228 ± 0.003	0.050 ± 0.005	0.251 ± 0.005	2716/48
		$\lvert\eta\rvert < 0.8$	5–10%	6.7 ± 0.2	0.227 ± 0.003	0.048 ± 0.005	0.250 ± 0.005	2292/48
		Pb–Pb	10–20%	6.5 ± 0.2	0.225 ± 0.003	0.046 ± 0.005	0.248 ± 0.005	2239/48
			20–30%	6.3 ± 0.2	0.221 ± 0.003	0.042 ± 0.005	0.246 ± 0.005	1814/48
			30–40%	6.2 ± 0.2	0.218 ± 0.003	0.039 ± 0.005	0.244 ± 0.005	1468/48
			40–50%	5.9 ± 0.2	0.215 ± 0.003	0.035 ± 0.005	0.238 ± 0.005	996/48
			50–60%	5.7 ± 0.2	0.211 ± 0.003	0.032 ± 0.005	0.231 ± 0.005	621/48
			60–70%	5.5 ± 0.2	0.209 ± 0.003	0.029 ± 0.005	0.227 ± 0.005	267/48
			70–80%	5.3 ± 0.2	0.207 ± 0.003	0.027 ± 0.005	0.224 ± 0.005	219/48
			80–90%	5.1 ± 0.2	0.204 ± 0.003	0.023 ± 0.005	0.221 ± 0.005	487/48
Figure 2(b)	$\left(K^{*0} + \bar{K}^{*0}\right)/2$	5.02	0–10%	7.0 ± 0.2	0.180 ± 0.003	1.028 ± 0.010	0.313 ± 0.006	103/10
		$\lvert y\rvert < 0.5$	10–20%	6.8 ± 0.2	0.176 ± 0.003	1.034 ± 0.010	0.309 ± 0.006	81/10
		Pb–Pb	20–30%	6.6 ± 0.2	0.173 ± 0.003	1.018 ± 0.010	0.305 ± 0.006	95/10
			30–40%	6.5 ± 0.2	0.171 ± 0.003	1.015 ± 0.010	0.302 ± 0.006	72/10
			40–50%	6.4 ± 0.2	0.171 ± 0.003	1.011 ± 0.010	0.300 ± 0.006	88/10
			50–60%	6.3 ± 0.2	0.168 ± 0.003	1.008 ± 0.010	0.298 ± 0.006	66/10
			60–70%	6.2 ± 0.2	0.166 ± 0.003	1.005 ± 0.010	0.297 ± 0.006	74/9
			70–80%	6.2 ± 0.2	0.164 ± 0.003	1.000 ± 0.010	0.295 ± 0.006	32/8
Figure 2(c)	ϕ	5.02	0–10%	8.1 ± 0.2	0.184 ± 0.003	1.017 ± 0.010	0.302 ± 0.006	323/19
		$\lvert y\rvert < 0.5$	10–20%	8.0 ± 0.2	0.182 ± 0.003	1.014 ± 0.010	0.301 ± 0.006	137/19
		Pb–Pb	20–30%	7.9 ± 0.2	0.180 ± 0.003	1.009 ± 0.010	0.299 ± 0.006	144/19
			30–40%	7.7 ± 0.2	0.177 ± 0.003	1.006 ± 0.010	0.295 ± 0.006	87/19
			40–50%	7.6 ± 0.2	0.174 ± 0.003	1.002 ± 0.009	0.293 ± 0.006	77/18
			50–60%	7.4 ± 0.2	0.169 ± 0.003	0.996 ± 0.009	0.291 ± 0.006	12/16
			60–70%	7.2 ± 0.2	0.165 ± 0.003	0.991 ± 0.009	0.288 ± 0.006	16/16
			70–80%	6.9 ± 0.2	0.158 ± 0.003	0.987 ± 0.009	0.285 ± 0.006	16/15

where the sums are considered due to the contributions of 2 or 3 quarks; the upper limit "2" for the sums corresponds to the meson, and the limit "3" for the sums corresponds to the baryon in the first two relations in Equation (6).

According to the above analysis, we may obtain a lot of discrete values of p_T by the iterative calculations. Finally, we may perform a statistical analysis on the discrete values of p_T and obtain suitable distributions such as $(1/2\pi p_T)d^2N/\mathrm{dydp}_T$ and d^2N/dydp_T, which can be compared with the experimental data, where y denotes the rapidity, and dy is the width of rapidity bin at midrapidity. In calculations, the statistical interval of p_T is taken to be 0.1 GeV/c.

Although we may simply use the modified Tsallis–Pareto-type function to fit the experimental data and adopt the χ^2-minimisation scheme to obtain the fit parameters, the results obtained by the simple method are at the particle level, which seem not to be deeper insight compared to the results at the quark and gluon level. To obtain the results at the partonic-level, we may consider the contribution of multiple partons to particle's transverse momentum. However, the analytical expression obtained at the partonic-level is not available due to the complex calculations for the superposition of multiple transverse momenta with randomized azimuthal angles. Instead, we may use the Monte Carlo method to obtain numerical results. This is suitable for the case discussed in this paper.

It should be noted that several restrictions are used in the Monte Carlo calculations. *First*, the constituent masses of the considered quarks are determinate. These masses are taken from the literature [38]. *Second*, p_{Ti} of a quark is restricted to obey a given function. This function is modified from the current Tsallis-like function. *Third*, an isotropic emission in the rest frame of emission source is assumed. The momentum in the rest frame of emission source is then obtained. *Fourth*, the movement of emission source is restricted by its rapidity which is assumed to be evenly distributed in the projectile or target thermalized region in the rapidity space. The rapidity of emission source is also

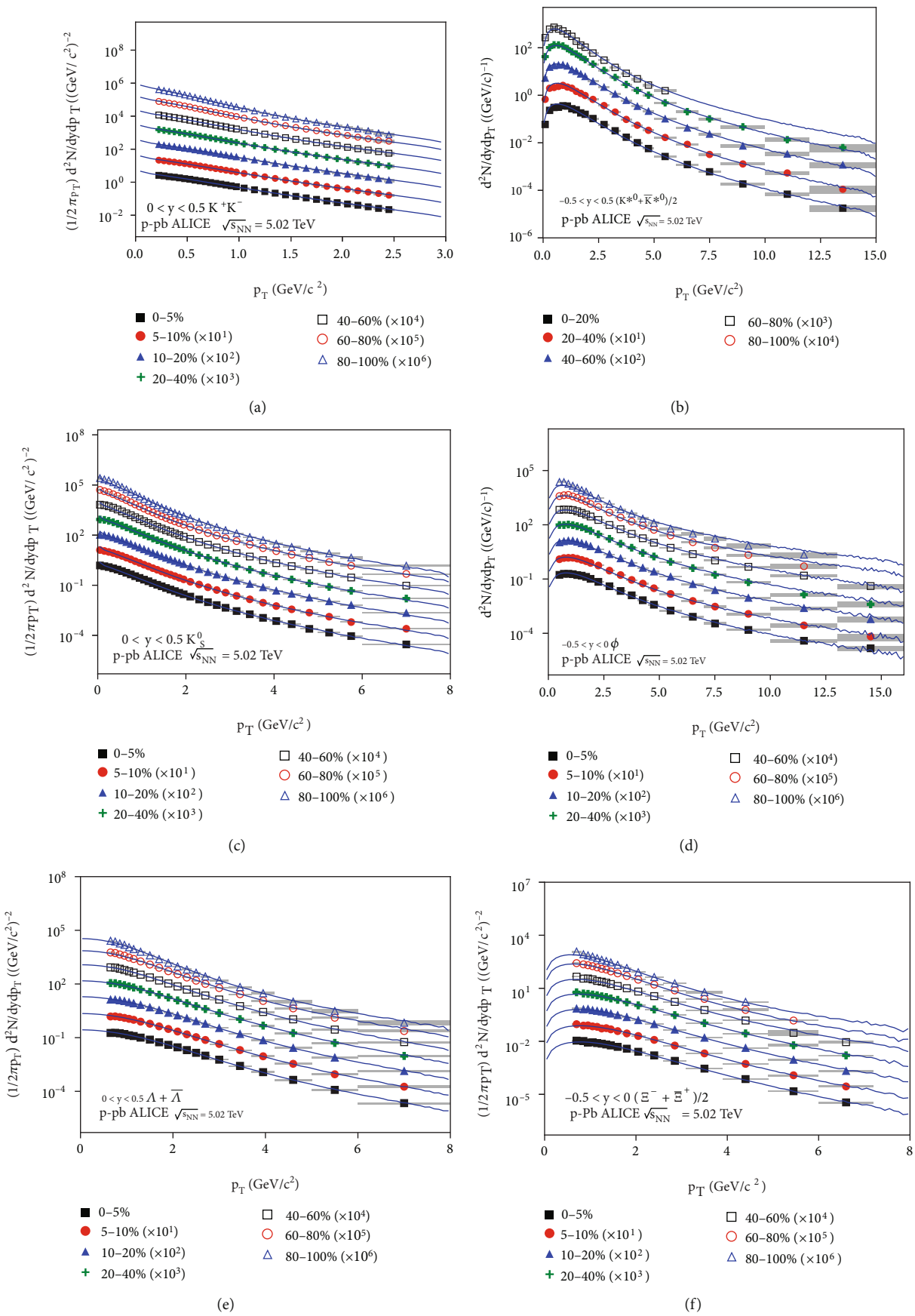

Figure 3: Continued.

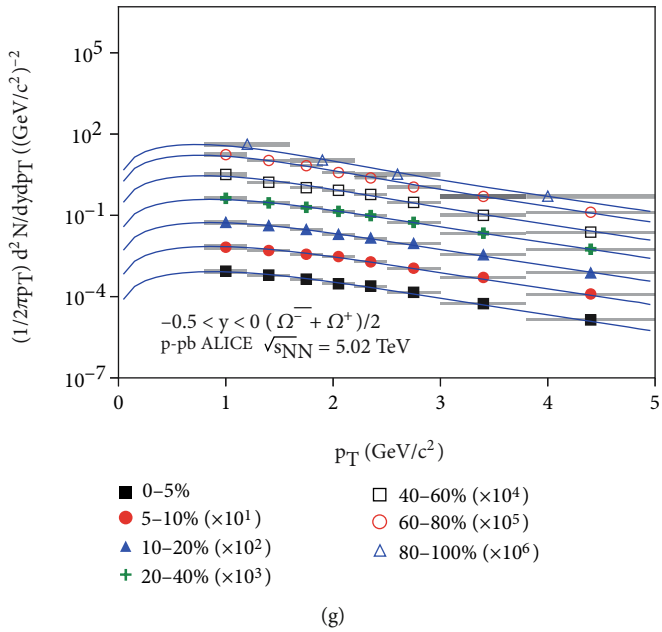

(g)

FIGURE 3: The p_T spectra of (a) $K^+ + K^-$, (b) $(K^{*0} + \bar{K}^{*0})/2$, (c) K^0_S, (d) ϕ, (e) $\Lambda + \bar{\Lambda}$, (f) $(\Xi^- + \bar{\Xi}^+)/2$, and (g) $(\Omega^- + \bar{\Omega}^+)/2$ in p–Pb collisions at $\sqrt{s_{NN}} = 5.02$ TeV. The symbols represent the data measured by the ALICE Collaboration [44, 45]. The solid curves represent the Monte Carlo results, based on the probability density function Equation (2) and the p_T expression in Equation (6).

related to longitudinal flow, which restricts the rapidity range. *Fifth*, the conservation of energy and momentum is obeyed. The combination of p_{Ti} of 2- or 3-quarks with randomized azimuthal angles into p_T of hadron can be conducted, in which any energy beyond hadron's rest mass is converted into hadron's kinetic energy. *Sixth*, the distribution of p_T is restricted by the experimental data.

3. Results and Discussion

3.1. Comparison with Data. In the study, we analyze the p_T spectra of strange particles generated in high energy lead–lead (Pb–Pb), proton–lead (p–Pb), and xenon–xenon (Xe–Xe) collisions at the Large Hadron Collider (LHC). Figure 1 shows the p_T spectra of (a) $K^+ + K^-$, (b) $(K^{*0} + \bar{K}^{*0})/2$, (c) K^0_S, (d) ϕ, (e) Λ, (f) Ξ^-, (g) $\bar{\Xi}^+$, (h) Ω^-, and (i) $\bar{\Omega}^+$ produced in Pb–Pb collisions with different centrality intervals marked in the panels at the collision energy $\sqrt{s_{NN}} = 2.76$ TeV per nucleon pair. The symbols represent the data measured by the ALICE Collaboration [39–41]. The mid-pseudorapidity range of panel (a) is $|\eta| < 0.2$, and those of other panels are $|y| < 0.5$. For better distinguishing and comparing, the data with different centralities in different panels are multiplied by 10 to the n-th power. In addition, the gray rectangles represent the uncertainty of the experimental data, whose length is the uncertainty of the abscissa, whereas the width is the uncertainty of the ordinate, which denote the quadratic sum of the statistical and systematical uncertainties. The solid curves represent the Monte Carlo results calculated from the probability density function in Equation (2) and the p_T expression in Equation (6).

We use $\chi^2 = \Sigma_j[(\text{Data}_j - \text{Fit}_j)^2/\text{Uncertainty}_j^2]$ to quantify the deviation of the Monte Carlo results from the experimental data, where j denotes the order number of the data. The smaller the mean of χ^2 is, the closer the Monte Carlo results to the experimental data are. The free parameters, the entropy-related index n, the kinetic freeze-out temperature T_0, the correction index a_0, and the average transverse flow velocity $\langle\beta_t\rangle$ are extracted by the method of least squares. The values of free parameters, χ^2 and the number of degree of freedom (ndof) are listed in Table 1. One can see that in most cases the Monte Carlo results agree well or approximately with the experimental p_T spectra of strange particles. In few cases, the Monte Carlo results are in qualitative agreement with the experimental data, for which the values of χ^2/ndof are quite large.

The p_T spectra of (a) $K^+ + K^-$, (b) $(K^{*0} + \bar{K}^{*0})/2$, and (c) ϕ are displayed in Figure 2 for Pb–Pb collisions at $\sqrt{s_{NN}} = 5.02$ TeV, quoted from the ALICE Collaboration [42, 43]. The mid-pseudorapidity is $|\eta| < 0.2$ in panel (a) and $|y| < 0.5$ in panels (b) and (c). Similarly to Figure 1, the data with different centralities are represented by different symbols, and the gray rectangles represent the uncertainty of the data. The solid curves show the Monte Carlo results. For clarity, we use a power index amplification from 10^1 to 10^9. The free parameters n, T_0, a_0, and $\langle\beta_t\rangle$, as well as χ^2/nd of are listed in Table 2. One can see that the Monte Carlo results show an approximate agreement with the data in some cases and a qualitative agreement with the data in the other cases.

In addition to Pb–Pb collisions, the experimental p_T spectra in other collisions are also studied in order to better explore the properties of strange particles. Figure 3 shows

Table 3: Values of n, T_0, a_0, $\langle\beta_t\rangle$, χ^2, and ndof corresponding to the solid curves in Figure 3.

Figure	Particle	$\sqrt{s_{\mathrm{NN}}}$ (TeV)	Selection	n	T_0 (GeV)	a_0	$\langle\beta_t\rangle$ (c)	χ^2/ndof
Figure 3(a)	$K^+ + K^-$	5.02	0–5%	5.5 ± 0.2	0.223 ± 0.003	0.229 ± 0.005	0.257 ± 0.005	7/26
		$0 < y < 0.5$	5–10%	5.3 ± 0.2	0.215 ± 0.003	0.226 ± 0.005	0.252 ± 0.005	6/26
		p–Pb	10–20%	5.1 ± 0.2	0.210 ± 0.003	0.221 ± 0.005	0.248 ± 0.005	4/26
			20–40%	4.9 ± 0.2	0.199 ± 0.003	0.214 ± 0.005	0.241 ± 0.005	3/26
			40–60%	4.7 ± 0.2	0.188 ± 0.003	0.205 ± 0.005	0.230 ± 0.005	2/26
			60–80%	4.5 ± 0.2	0.167 ± 0.003	0.197 ± 0.005	0.221 ± 0.005	2/26
			80–100%	4.3 ± 0.2	0.139 ± 0.003	0.183 ± 0.005	0.212 ± 0.005	5/26
Figure 3(b)	$\left(K^{*0} + \bar{K}^{*0}\right)/2$	5.02	0–20%	6.8 ± 0.2	0.238 ± 0.003	0.550 ± 0.007	0.267 ± 0.005	72/17
		$-0.5 < y < 0$	20–40%	6.7 ± 0.2	0.231 ± 0.003	0.541 ± 0.007	0.258 ± 0.005	56/17
		p–Pb	40–60%	6.4 ± 0.2	0.225 ± 0.003	0.536 ± 0.007	0.254 ± 0.005	16/17
			60–80%	6.2 ± 0.2	0.211 ± 0.003	0.528 ± 0.007	0.249 ± 0.005	11/17
			80–100%	5.7 ± 0.2	0.183 ± 0.003	0.511 ± 0.007	0.233 ± 0.005	19/12
Figure 3(c)	K_S^0	5.02	0–5%	6.6 ± 0.2	0.219 ± 0.003	0.202 ± 0.005	0.328 ± 0.006	78/29
		$0 < y < 0.5$	5–10%	6.5 ± 0.2	0.216 ± 0.003	0.200 ± 0.005	0.325 ± 0.006	39/29
		p–Pb	10–20%	6.4 ± 0.2	0.214 ± 0.003	0.199 ± 0.005	0.323 ± 0.006	55/29
			20–40%	6.2 ± 0.2	0.209 ± 0.003	0.197 ± 0.005	0.321 ± 0.006	45/29
			40–60%	6.0 ± 0.2	0.204 ± 0.003	0.192 ± 0.005	0.317 ± 0.006	61/29
			60–80%	5.7 ± 0.2	0.189 ± 0.003	0.186 ± 0.005	0.312 ± 0.006	83/29
			80–100%	5.8 ± 0.2	0.174 ± 0.003	0.184 ± 0.005	0.304 ± 0.006	145/29
Figure 3(d)	ϕ	5.02	0–5%	6.7 ± 0.2	0.199 ± 0.003	0.812 ± 0.009	0.332 ± 0.006	18/15
		$-0.5 < y < 0$	5–10%	6.6 ± 0.2	0.197 ± 0.003	0.810 ± 0.009	0.330 ± 0.006	26/15
		p–Pb	10–20%	6.4 ± 0.2	0.194 ± 0.003	0.806 ± 0.009	0.324 ± 0.006	29/15
			20–40%	6.3 ± 0.2	0.192 ± 0.003	0.803 ± 0.009	0.322 ± 0.006	25/15
			40–60%	6.1 ± 0.2	0.189 ± 0.003	0.799 ± 0.008	0.319 ± 0.006	20/15
			60–80%	5.5 ± 0.2	0.165 ± 0.003	0.783 ± 0.008	0.312 ± 0.006	38/14
			80–100%	5.1 ± 0.2	0.147 ± 0.003	0.775 ± 0.008	0.305 ± 0.006	63/14
Figure 3(e)	$\Lambda + \bar{\Lambda}$	5.02	0–5%	7.7 ± 0.2	0.132 ± 0.002	1.426 ± 0.012	0.226 ± 0.004	6/15
		$0 < y < 0.5$	5–10%	7.6 ± 0.2	0.130 ± 0.002	1.424 ± 0.012	0.224 ± 0.004	4/15
		p–Pb	10–20%	7.5 ± 0.2	0.127 ± 0.002	1.421 ± 0.012	0.221 ± 0.004	2/15
			20–40%	7.3 ± 0.2	0.123 ± 0.002	1.417 ± 0.012	0.218 ± 0.004	4/15
			40–60%	7.0 ± 0.2	0.112 ± 0.002	1.410 ± 0.012	0.211 ± 0.004	4/15
			60–80%	6.7 ± 0.2	0.104 ± 0.002	1.407 ± 0.012	0.206 ± 0.004	22/15
			80–100%	6.4 ± 0.2	0.089 ± 0.002	1.403 ± 0.012	0.202 ± 0.004	23/15
Figure 3(f)	$\left(\Xi^- + \bar{\Xi}^+\right)/2$	5.02	0–5%	9.0 ± 0.2	0.179 ± 0.003	0.703 ± 0.008	0.225 ± 0.004	15/12
		$-0.5 < y < 0$	5–10%	8.9 ± 0.2	0.177 ± 0.003	0.701 ± 0.008	0.223 ± 0.004	14/12
		p–Pb	10–20%	8.4 ± 0.2	0.171 ± 0.003	0.692 ± 0.008	0.218 ± 0.004	9/12
			20–40%	8.0 ± 0.2	0.165 ± 0.003	0.688 ± 0.008	0.215 ± 0.004	18/12
			40–60%	7.2 ± 0.2	0.150 ± 0.003	0.678 ± 0.008	0.209 ± 0.004	40/12
			60–80%	7.0 ± 0.2	0.130 ± 0.002	0.669 ± 0.008	0.203 ± 0.004	19/11
			80–100%	6.4 ± 0.2	0.119 ± 0.002	0.662 ± 0.008	0.194 ± 0.004	25/10

Table 3: Continued.

Figure	Particle	$\sqrt{s_{NN}}$ (TeV)	Selection	n	T_0 (GeV)	a_0	$\langle\beta_t\rangle$ (c)	χ^2/ndof
Figure 3(g)	$\left(\Omega^- + \bar{\Omega}^+\right)/2$	5.02	0–5%	7.6 ± 0.2	0.174 ± 0.003	0.788 ± 0.008	0.240 ± 0.005	5/3
		$-0.5 < y < 0$	5–10%	7.3 ± 0.2	0.173 ± 0.003	0.786 ± 0.008	0.238 ± 0.005	4/3
		p–Pb	10–20%	7.2 ± 0.2	0.170 ± 0.003	0.783 ± 0.008	0.235 ± 0.005	4/3
			20–40%	7.0 ± 0.2	0.167 ± 0.003	0.779 ± 0.008	0.232 ± 0.004	1/3
			40–60%	6.7 ± 0.2	0.150 ± 0.003	0.769 ± 0.008	0.223 ± 0.004	9/3
			60–80%	6.4 ± 0.2	0.141 ± 0.002	0.761 ± 0.008	0.214 ± 0.004	5/3
			80–100%	5.9 ± 0.2	0.132 ± 0.002	0.755 ± 0.008	0.206 ± 0.004	2/–

the p_T spectra of (a) $K^+ + K^-$, (b) $(K^{*0} + \bar{K}^{*0})/2$, (c) K^0_S, (d) ϕ, (e) $\Lambda + \bar{\Lambda}$, (f) $(\Xi^- + \bar{\Xi}^+)/2$, and (g) $(\Omega^- + \bar{\Omega}^+)/2$ in p–Pb collisions at $\sqrt{s_{NN}} = 5.02$ TeV. The experimental data in the panels are all quoted from the ALICE Collaboration when the midrapidity is $0 < y < 0.5$ (a, c, e) and $-0.5 < y < 0$ (b, d, f, g) [44, 45]. Different symbols indicate the different centrality intervals. The Monte Carlo results are given by the solid curves. The coefficients in parentheses are magnification factors for better distinguishing the spectra in different centrality intervals. The relevant parameters n, T_0, a_0, and $\langle\beta_t\rangle$, as well as χ^2/nd of are listed in Table 3. One can see that the Monte Carlo results are in good agreement with the data in most cases and approximately in agreement with the data in few cases.

Besides, we have also studied the p_T spectra of (a) $K^+ + K^-$ and (b) ϕ produced in Xe–Xe collisions at $\sqrt{s_{NN}} = 5.44$ TeV in Figure 4. The symbols represent the data measured by the ALICE Collaboration, and the mid-pseudorapidity is $|\eta| < 0.8$ [46]. Similarly, the data with different centralities are expressed as different symbols with gray rectangles, and the solid curves show the Monte Carlo results. Another, 10^n in legends are magnification factors for better distinguishing the spectra. The relevant parameters n, T_0, a_0, and $\langle\beta_t\rangle$, as well as χ^2/nd of are listed in Table 4. Once again, one can see that the Monte Carlo results are in good agreement with the experimental data.

3.2. Tendencies of Parameters. To further understand the regularities shown by the p_T spectra of strange particles, we analyze the tendencies of various parameters with changing centrality observed in the work. Figure 5 shows the dependence of entropy-related index (a, b) n on centrality and C in Pb–Pb, (c) p–Pb, and (d) Xe–Xe collisions at the LHC energies. The symbols are quoted from Tables 1–4, where the results from different particles are represented by different symbols. As an entropy-related index, $n = 1/(q - 1)$ or $n = q'/(q' - 1)$ describes the degree of nonequilibrium of the system, where q (q') is the entropy index. Generally, a larger n or a q (q') closer to 1 corresponds to a higher degree of equilibrium. The present work shows that n is large enough or q (q') is close to 1, and the system stays in an approximate equilibrium. Meanwhile, the system in central collisions stays in higher degree of equilibrium. In addition, as the rest mass of strange particle increases, the value of n increases. The multistrange particles correspond to larger n than the single-strange particles. These results imply that the system stays in larger degree of equilibrium when it forms multistrange particles.

Similar to Figure 5, Figure 6 shows the dependence of kinetic freeze-out temperature T_0 on centrality C in the mentioned collisions at the LHC. One can see that T_0 decreases slightly with the decrease of centrality from central to peripheral collisions in most cases. In few cases, the decrease is significant. In addition, T_0 extracted from the single-strange particle spectra is larger than that from the multistrange particle spectra. This finding suggests that the single-strange particles are formed earlier than the multistrange particles, though the latter may leave the system earlier than the former in the hydrodynamic evolution due to different masses.

As shown in Figure 7, we present the changing law of the correction index a_0 on centrality C in the mentioned collisions at the LHC. One can see that with the decrease of centrality from central to peripheral collisions, a_0 is almost invariant, though in few cases a_0 shows very slight decrease. In most cases, the values of a_0 are far from 1, which means that the introduction of a_0 is necessary. We have also compared the present fits with $a_0 \neq 1$ with those by $a_0 = 1$. An obvious difference appears in the low-p_T region. This implies that the fits by $a_0 = 1$ are not suitable. In fact, in the fits of the present work, we use $a_0 = 1$ at the first, then we change a_0 to fit the p_T spectra if $a_0 = 1$ is not satisfactory.

The dependence of the average transverse flow velocity $\langle\beta_t\rangle$ on centrality C in the mentioned collisions at the LHC is displayed in Figure 8. Similar conclusions to the dependences of n on C and T_0 on C can be obtained. That is, $\langle\beta_t\rangle$ decreases slightly with the decrease of centrality from central to peripheral collisions in most cases. In few cases, the decrease is significant. In addition, $\langle\beta_t\rangle$ extracted from the single-strange particle spectra is larger than that from the multistrange particle spectra. This finding also suggests that the single-strange particles are formed earlier than the multistrange particles.

In order to further study the final states of the strange particles and the disorder degree of the system, we give the results of pseudoentropy $S'_{\text{hadron}} = -\Sigma[f(p_T)/\Sigma f(p_T)] \ln [f(p_T)/\Sigma f(p_T)]$ [28], which is based on the probability density function $f(p_T)$ of p_T, inspired by the entropy

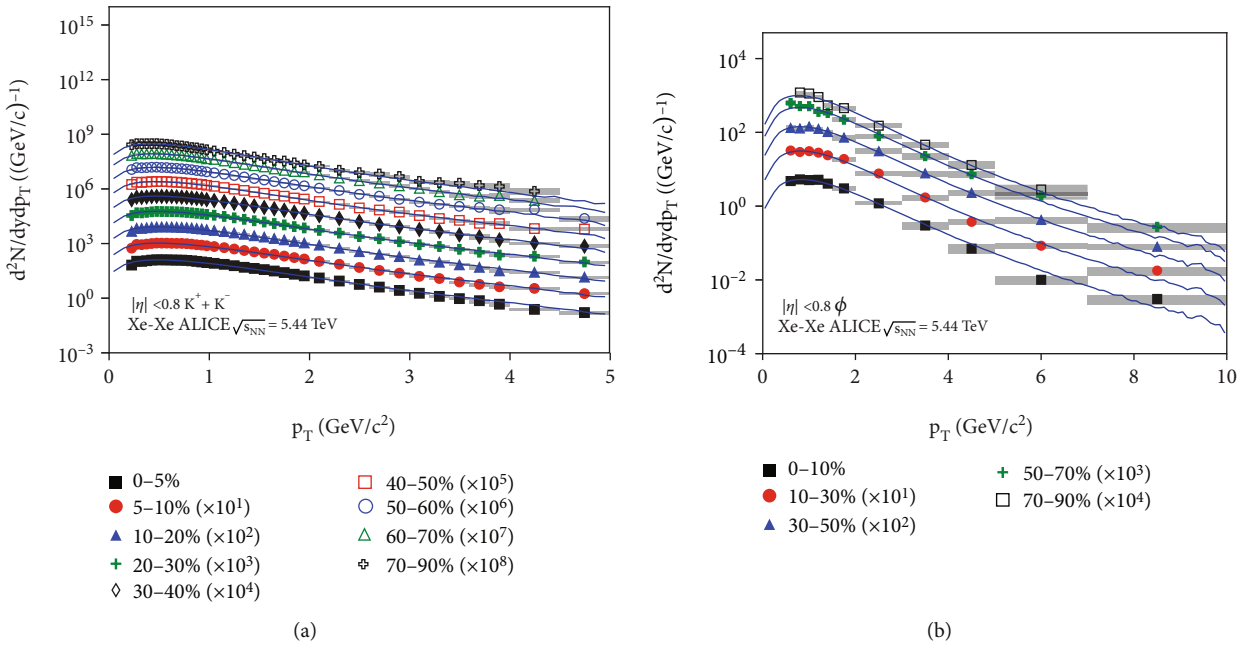

FIGURE 4: The p_T spectra of (a) $K^+ + K^-$ and (b) ϕ produced in Xe–Xe collisions at $\sqrt{s_{NN}} = 5.44$ TeV. The symbols represent the data measured by the ALICE Collaboration [46]. The solid curves represent the Monte Carlo results, based on the probability density function Equation (2) and the p_T expression in Equation (6).

TABLE 4: Values of n, T_0, a_0, $\langle\beta_t\rangle$, χ^2, and ndof corresponding to the solid curves in Figure 4.

Figure	Particle	$\sqrt{s_{NN}}$ (TeV)	Selection	n	T_0 (GeV)	a_0	$\langle\beta_t\rangle$ (c)	χ^2/ndof
Figure 4(a)	$K^+ + K^-$	5.44	0–5%	8.3 ± 0.2	0.199 ± 0.003	0.399 ± 0.006	0.257 ± 0.005	73/33
		$\|\eta\| < 0.8$	5–10%	8.1 ± 0.2	0.198 ± 0.003	0.396 ± 0.006	0.255 ± 0.005	58/33
		Xe–Xe	10–20%	7.9 ± 0.2	0.194 ± 0.003	0.395 ± 0.006	0.254 ± 0.005	55/33
			20–30%	7.7 ± 0.2	0.192 ± 0.003	0.392 ± 0.006	0.252 ± 0.005	37/33
			30–40%	7.5 ± 0.2	0.187 ± 0.003	0.390 ± 0.006	0.250 ± 0.005	20/33
			40–50%	7.3 ± 0.2	0.183 ± 0.003	0.386 ± 0.006	0.247 ± 0.005	16/33
			50–60%	7.2 ± 0.2	0.179 ± 0.003	0.384 ± 0.006	0.244 ± 0.005	14/33
			60–70%	7.1 ± 0.2	0.174 ± 0.003	0.381 ± 0.006	0.238 ± 0.005	16/32
			70–90%	6.9 ± 0.2	0.162 ± 0.003	0.368 ± 0.006	0.230 ± 0.005	27/32
Figure 4(b)	ϕ	5.44	0–10%	9.0 ± 0.2	0.219 ± 0.003	0.810 ± 0.009	0.338 ± 0.006	13/6
		$\|\eta\| < 0.8$	10–30%	8.9 ± 0.2	0.216 ± 0.003	0.804 ± 0.009	0.334 ± 0.006	10/6
		Xe–Xe	30–50%	8.7 ± 0.2	0.213 ± 0.003	0.800 ± 0.008	0.332 ± 0.006	7/6
			50–70%	8.5 ± 0.2	0.209 ± 0.003	0.797 ± 0.008	0.327 ± 0.006	11/6
			70–90%	8.3 ± 0.2	0.203 ± 0.003	0.792 ± 0.008	0.317 ± 0.006	10/4

$S_{\text{hadron}} = -\Sigma P(N) \ln P(N)$ [47–49], based on the probability density function $P(N)$ of multiplicity N, where p_T is in the units of GeV/c. As is done in our recent work [24], the width of p_T bin is taken to be 0.1 GeV/c, though the width is changeable. The unit of $f(p_T)$ is neglected due to the fact that $P(N)$ is dimensionless.

In Figure 9, we demonstrate the relation of the pseudoentropy S'_{hadron} versus the centrality C. It is seen from the results that S'_{hadron} decreases slightly with the decrease of centrality from central to peripheral collisions in most cases. Only in few cases, S'_{hadron} decreases significantly with the decrease of C. The dependence of S'_{hadron} on C is similar to those of n, T_0, and $\langle\beta_t\rangle$ on C. Generally, the multistrange particles show larger S'_{hadron} than the single-strange particles, though both S'_{hadron} for multi and single-strange particles are

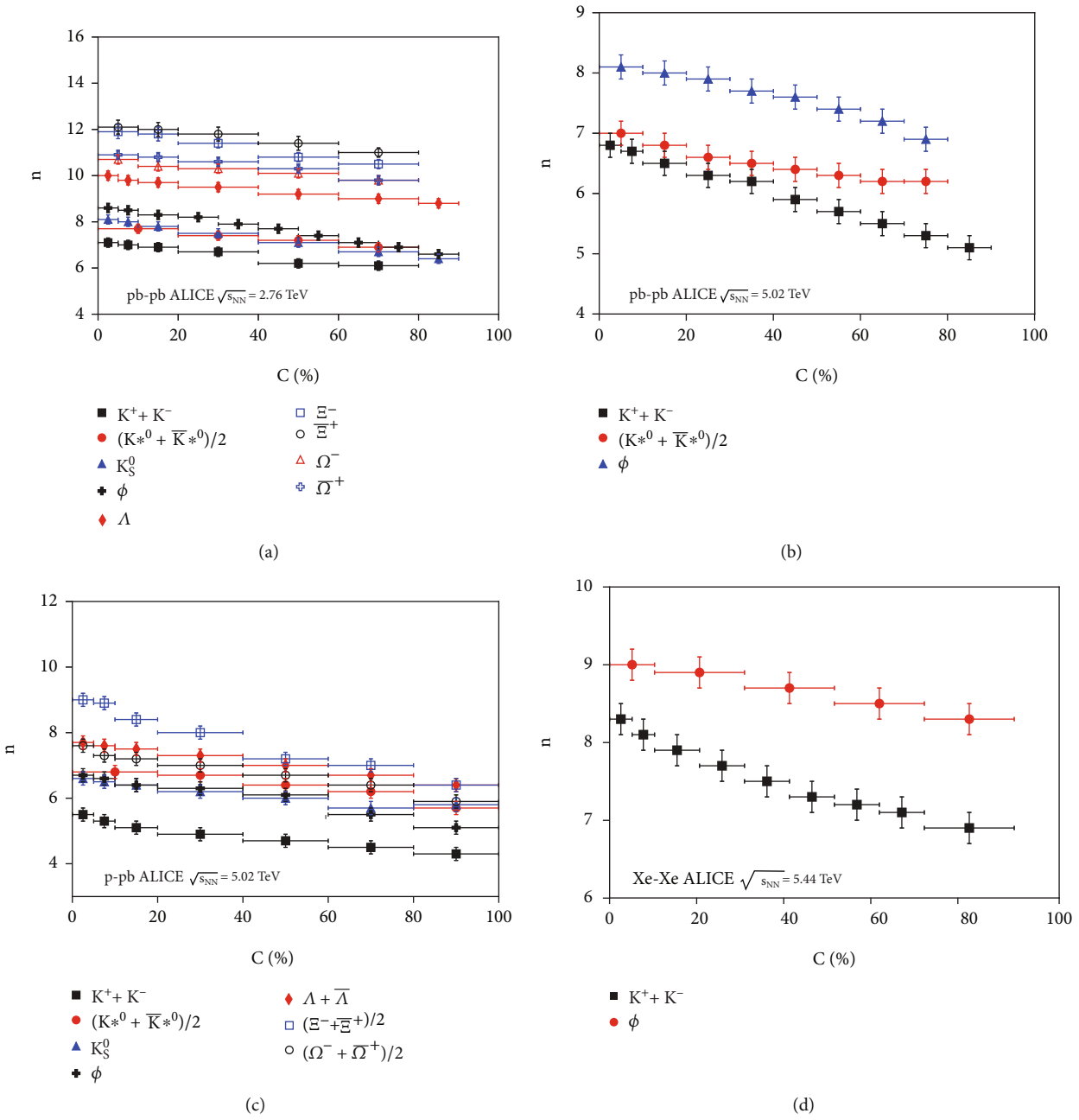

Figure 5: Dependence of entropy-related index (a, b) n on centrality and C in Pb–Pb, (c) p–Pb, and (d) Xe–Xe collisions.

negative. This also reflects the mass-dependence of S'_{hadron}, which is similar to those of the other parameters.

Analyzing Figures 5–9, one can see that the correlations between n and T_0, n and $\langle\beta_t\rangle$, n and S'_{hadron}, T_0 and $\langle\beta_t\rangle$, T_0 and S'_{hadron}, and $\langle\beta_t\rangle$ and S'_{hadron} are positive; while the correlations between a_0 and n, a_0 and T_0, a_0 and $\langle\beta_t\rangle$, and a_0 and S'_{hadron} are very small or negligible. These results are understandable due to the fact that all n, T_0, and $\langle\beta_t\rangle$ determine mainly, and S'_{hadron} is mostly defined by, the shape of the spectra in intermediate- and high-p_T regions; while a_0 determines mainly the spectra in low- or even very low-p_T region. Of course, because of the requirement of normalization, all parameters affect the spectra in the whole p_T region, though the level of influence in different p_T regions are different.

3.3. Further Discussion. Although the extraction of T_0 and $\langle\beta_t\rangle$ in present work is performed at the partonic-level, most extractions in the literature have been done at the particle level, showing inconsistent trends. For example, in terms of dependence of parameters on centrality from central to peripheral collisions, some works show an increase in T_0 and a decrease in $\langle\beta_t\rangle$, and $\langle\beta_t\rangle \approx 0$ in small system or peripheral collisions [50–52]. Other work shows a decrease in both T_0 and $\langle\beta_t\rangle$, and $\langle\beta_t\rangle$ is considerable in small system or peripheral collisions [53]. Generally, the relative difference

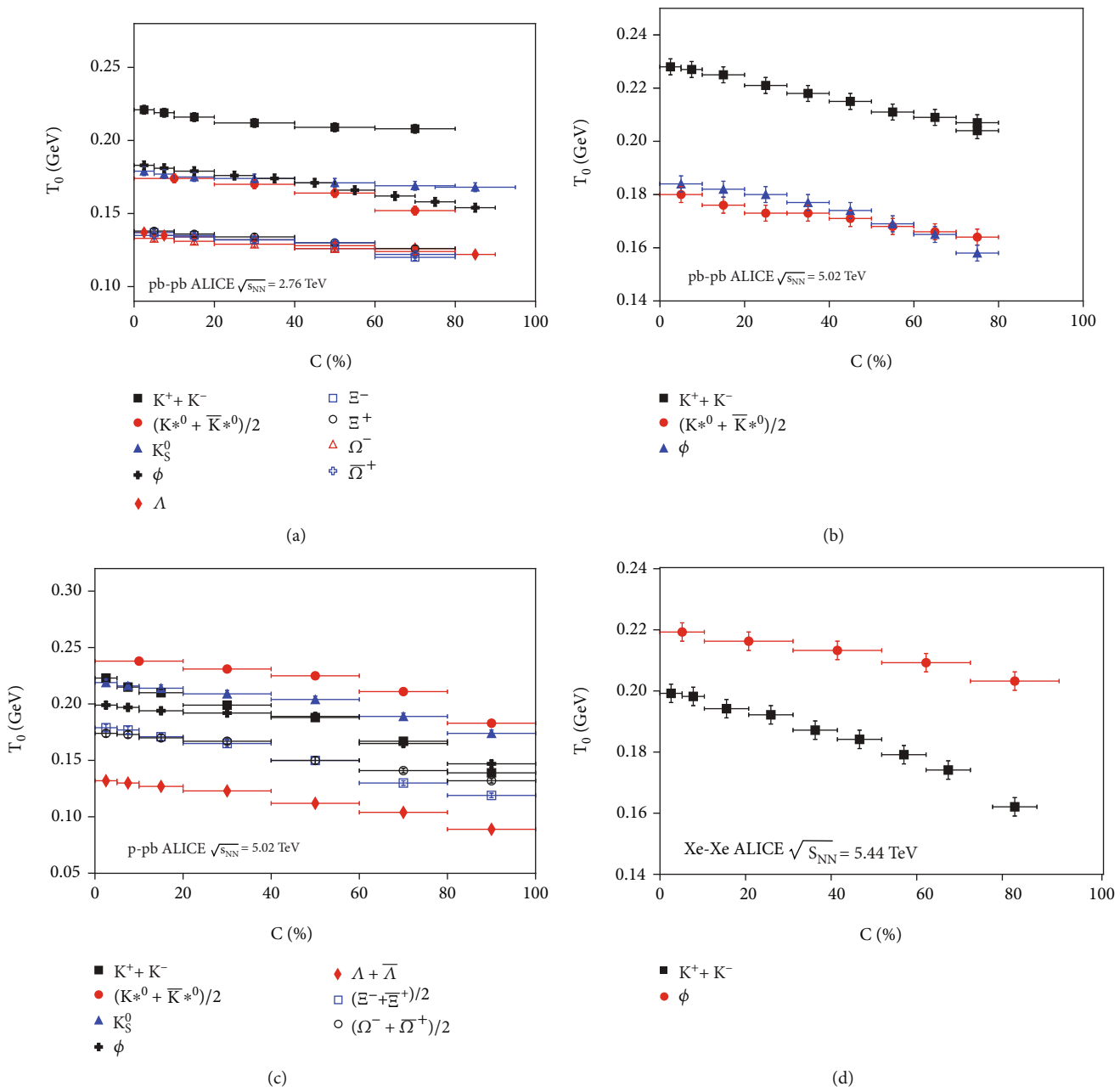

FIGURE 6: Dependence of kinetic freeze-out temperature (a, b) T_0 on centrality and C in Pb–Pb, (c) p–Pb, and (d) Xe–Xe collisions.

between two T_0 in central and peripheral collisions is small (~ 10%).

We observe a slightly higher T_0 in central collisions at both the partonic- and particle level. If so, the centrality dependence of T_0 is similar to those of the chemical freeze-out temperature and effective temperature. However, it is still an open question which T_0 is larger. In any case, the explanation is understandable. A higher T_0 in central collisions means a higher excitation, and a lower T_0 in central collisions means a longer lifetime, of the hot and dense matter. Although we may extract the thermal parameters at the particle level, we aim to perform it at the partonic-level. The reason is that the similarity, commonality, and universality available in high energy collisions [54–61] should be related to partons, which are a deeper level in the structure of matter compared to the particle level.

The present work shows that central collisions correspond to a higher excitation degree and a larger blast due to the more energy being deposited. Meanwhile, central collisions correspond to higher degree of equilibrium due to many particles being produced. Compared with the parameters at the particle level, the parameters at the partonic-level are extracted at earlier time moment and correspond to larger T_0 and $\langle\beta_t\rangle$. However, the system at the particle level is at higher degree of equilibrium due to the fact that longer time is taken to approach the chemical and kinetic

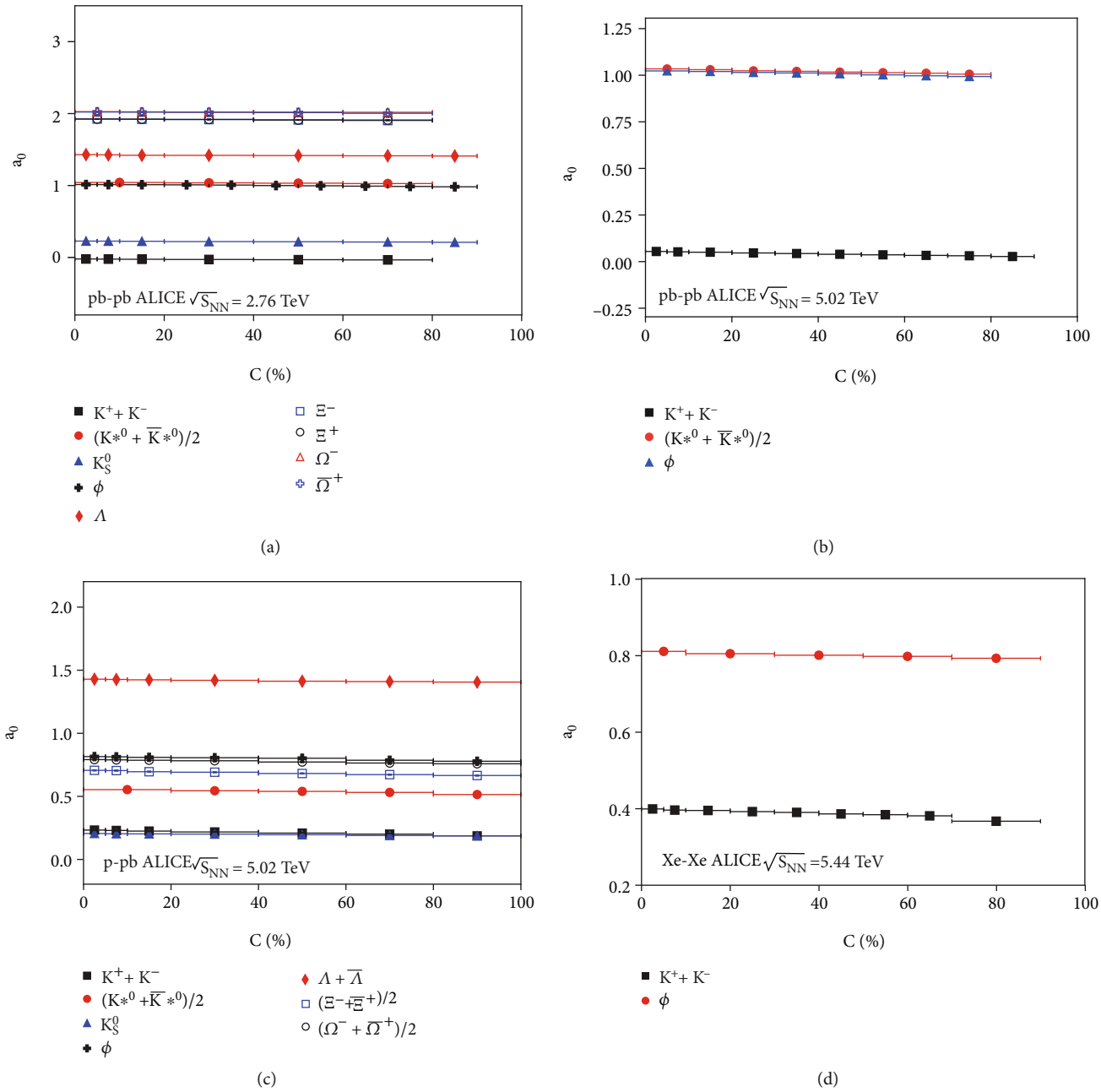

Figure 7: Dependence of correction index (a, b) a_0 on centrality and C in Pb–Pb, (c) p–Pb, and (d) Xe–Xe collisions.

freeze-out. However, because the time span from parton phase to particle phase is very small, the difference between two sets of parameters at the partonic- and particle level is very small.

In some cases, the fitting quality is not so good due to large χ^2 values. This is because only experimental uncertainty is considered. In fact, we have used the Monte Carlo method, which causes additional uncertainty. If we take the uncertainty induced by the Monte Carlo method to be approximately the same as the experimental uncertainty, χ^2 values will be reduced by $1/\sqrt{2} \approx 70.7\%$. In the case of large χ^2 values, we may regard the fits as the qualitative ones. In most cases, the fits are good or approximate, and in few cases the fits are qualitative.

Before summarizing and concluding, we would like to conduct some further discussions on the Monte Carlo results. As we know, most of baryons consist of up and down quarks, and the number of strange quarks is very small. Only when there is a formation of QGP, the system is likely to produce a lot of strange quarks and strange antiquarks, and then, strange quarks and strange antiquarks are able to combine with other neighbouring partons to form strange particles. Thus, the abundant yield of the final-state strange particles is an important signal of the existence of QGP

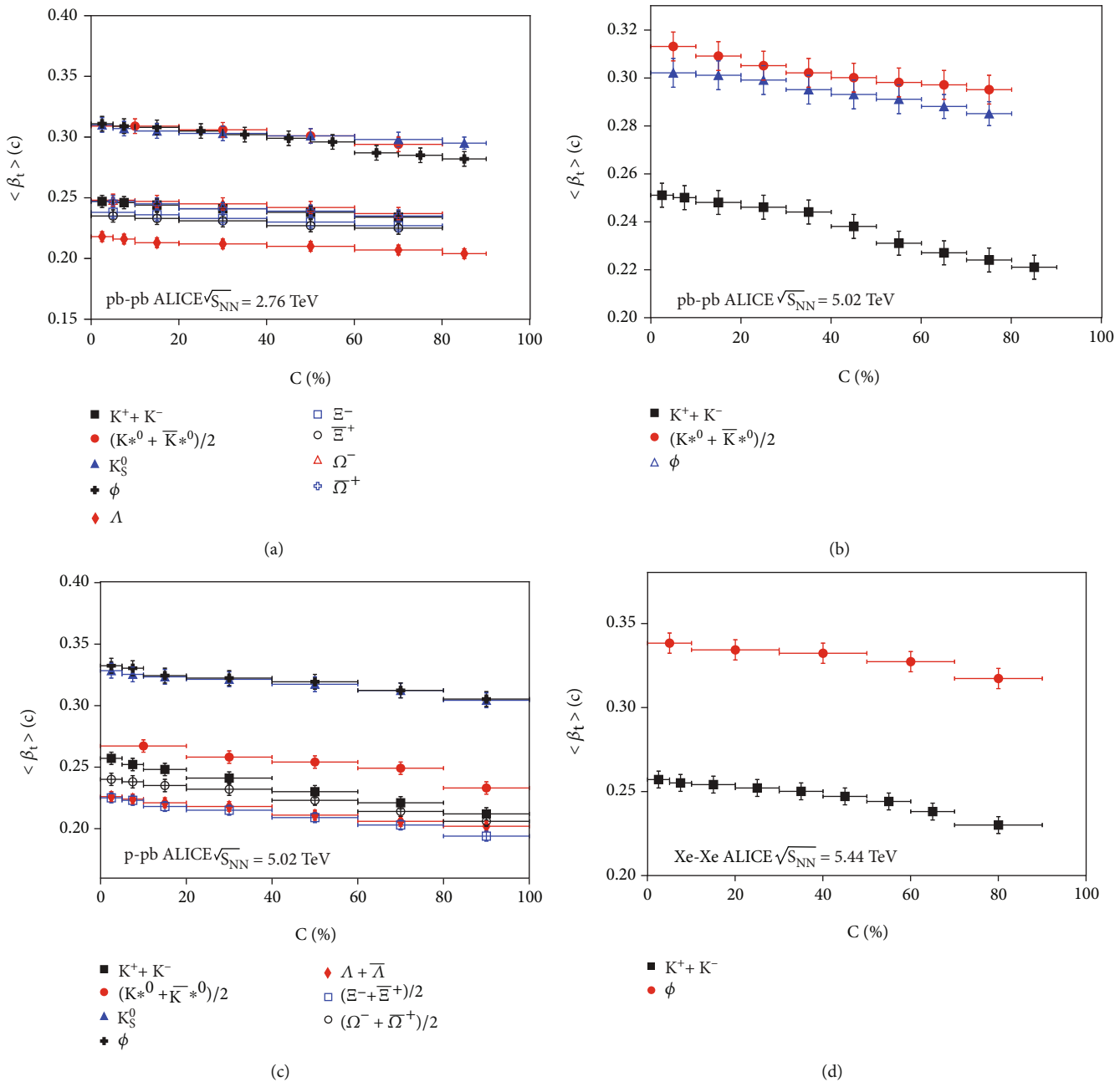

Figure 8: Dependence of average transverse flow velocity (a, b) $\langle \beta_t \rangle$ on centrality and C in Pb–Pb, (c) p–Pb, and (d) Xe–Xe collisions.

matter [62–67]. Because of the formation of QGP with abundance of strange particles, the implementation of this work has become possible due to sufficient statistics.

In the above discussions, we have used different sets of the parameters to fit the p_T spectra of different strange particles. This means that we have used the multiscenario of kinetic freeze-out. In some cases, the two-scenario of kinetic freeze-out is also applicable, if we consider the single-strange and multistrange particles, respectively. In our opinion, the single-scenario is a rough description, the two-scenario is a slight refined description, and the multiple-scenario is a more refined description, of the process of kinetic freeze-out. This situation is analogous to the atomic spectra and their fine structures.

4. Summary and Conclusions

The transverse momentum spectra of strange particles, including $K^{\pm}$, ϕ, Ω, Ξ, and so on, in high energy collisions are analyzed by considering the contributions of constituent quarks. Each constituent quark contributes to the transverse momentum obeying the modified Tsallis–Pareto-type function with random azimuthal angle. The transverse momentum of strange particle is the vector superposition of the

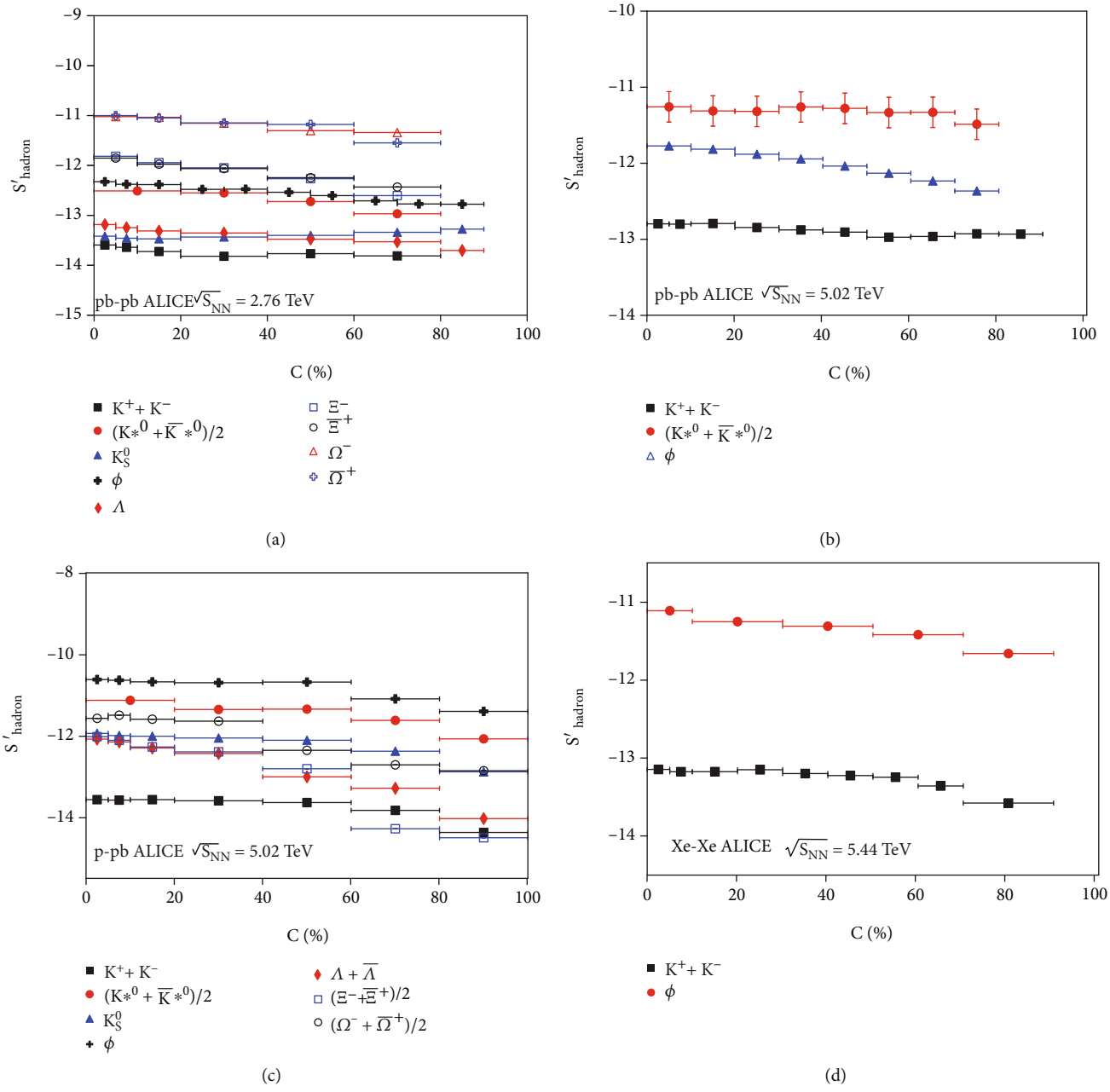

FIGURE 9: Dependence of pseudoentropy (a, b) S'_{hadron} on centrality C in Pb–Pb, (c) p–Pb, and (d) Xe–Xe collisions.

transverse momenta of the two or three constituent quarks. The results calculated by the Monte Carlo method are in good agreement with the experimental data in most cases in Pb–Pb, p–Pb, and Xe–Xe collisions at a few TeV, measured by the ALICE Collaboration at the LHC. In few cases, the agreement is qualitative due to quite large χ^2 values.

With the decrease of centrality from central to peripheral collisions, the free parameters n, T_0, and $\langle\beta_t\rangle$, as well as the derived parameter S'_{hadron} decrease slightly in most cases and decrease significantly in few cases. Meanwhile, the free parameter a_0 is almost invariant in most cases and decreases slightly in few cases. These results imply that central collisions stay in the state with larger degree of equilibrium, higher excitation, and larger blast than peripheral collisions, though both the central and peripheral collisions stay in approximate equilibrium when the system produces a lot of strange particles.

The correlations between n and T_0, n and $\langle\beta_t\rangle$, n and S'_{hadron}, T_0 and $\langle\beta_t\rangle$, T_0 and S'_{hadron}, and $\langle\beta_t\rangle$ and S'_{hadron} are positive, because all n, T_0, and $\langle\beta_t\rangle$ determine mainly, and S'_{hadron} is mostly defined by the shape of the spectra in intermediate- and high-p_T regions. The correlations between a_0 and n, a_0 and T_0, a_0 and $\langle\beta_t\rangle$, and a_0 and S'_{hadron} are very

small or negligible, because a_0 determines mainly the spectra in (very) low-p_T region.

We have used the multiscenario of kinetic freeze-out, though in some cases the two-scenario of kinetic freeze-out may also be applicable if we consider a part of p_T region. Meanwhile, if we consider the single-strange and multistrange particles, respectively, the single-strange particles are shown to form earlier than the multistrange ones. We may regard the relations of various scenarios as follows: the single-scenario is a rough description, the two-scenario is a slightly refined description, and the multiple-scenario is a more refined description of the process of kinetic freeze-out.

Data Availability

The data used to support the findings of this study are included within the article and are cited at relevant places within the text as references.

Ethical Approval

The authors declare that they are in compliance with ethical standards regarding the content of this paper.

Disclosure

The funding agencies have no role in the design of the study; in the collection, analysis, or interpretation of the data; in the writing of the manuscript or in the decision to publish the results. A preprint has previously been published [68].

Conflicts of Interest

The authors declare that there are no conflicts of interest regarding the publication of this paper.

Acknowledgments

The work of X.-H.Z. was supported by the Innovative Foundation for Graduate Education in Shanxi University. The work of Shanxi Group was supported by the National Natural Science Foundation of China under Grant Nos. 12147215, 12047571, and 11575103; the Shanxi Provincial Natural Science Foundation under Grant Nos. 202103021224036 and 201901D111043; the Scientific and Technological Innovation Programs of Higher Education Institutions in Shanxi (STIP) under Grant No. 201802017, the Fund for Shanxi "1331 Project" Key Subjects Construction. The work of Kh.K.O. was supported by the Ministry of Innovative Development of the Republic of Uzbekistan within the fundamental project No. F3-20200929146 on analysis of open data on heavy-ion collisions at RHIC and LHC. The work of A.D. was partially supported by the Conselho Nacional de Desenvolvimento Científico e Tecnológico (CNPq-Brazil), by Project INCT-FNA Proc. No. 464 898/2014-5, and by FAPESP under grant 2016/17612-7.

References

[1] K. Adcox, S. S. Adler, S. Afanasiev et al., "Formation of dense partonic matter in relativistic nucleus-nucleus collisions at RHIC: experimental evaluation by the PHENIX collaboration," *Nuclear Physics A*, vol. 757, no. 1–2, pp. 184–283, 2005.

[2] J. Adams, M. M. Aggarwal, Z. Ahammed et al., "Experimental and theoretical challenges in the search for the quark-gluon plasma: the STAR collaboration's critical assessment of the evidence from RHIC collisions," *Nuclear Physics A*, vol. 757, no. 1-2, pp. 102–183, 2005.

[3] H. Satz and R. Stock, "Quark matter: the beginning," *Nuclear Physics A*, vol. 956, pp. 898–901, 2016.

[4] B. Liu, M. Di Toro, G. Y. Shao, V. Greco, C. W. Shen, and Z. H. Li, "Hadron-quark phase coexistence in a hybrid MIT-bag model," *The European Physical Journal A*, vol. 47, no. 9, article 104, 2011.

[5] M. Cacciari, P. Nason, and R. Vogt, "QCD predictions for charm and bottom quark production at RHIC," *Physical Review Letters*, vol. 95, no. 12, article 122001, 2005.

[6] Z. W. Lin and M. Gyulassy, "Open charm as a probe of preequilibrium dynamics in nuclear collisions," *Physical Review C*, vol. 51, no. 4, pp. 2177–2187, 1995.

[7] G. R. Che, J. B. Gu, W. C. Zhang, and H. Zheng, "Identified particle spectra in Pb-Pb, Xe-Xe and p-Pb collisions with the Tsallis blast-wave model," *Journal Physical G*, vol. 48, no. 9, article 095103, 2021.

[8] J. Chen, J. Deng, Z. B. Tang, Z. B. Xu, and L. Yi, "Nonequilibrium kinetic freeze-out properties in relativistic heavy ion collisions from energies employed at the RHIC beam energy scan to those available at the LHC," *Physical Review C*, vol. 104, no. 3, article 034901, 2021.

[9] Y. Su, Y.-J. Sun, Y.-F. Zhang, and X.-L. Chen, "Non-extensive statistical distribution of charmed meson production in Pb-Pb and pp($\bar{\text{p}}$) collisions," *Nuclear Science and Techniques*, vol. 32, no. 10, article 108, 2021.

[10] J. Adam, D. Adamova, M. M. Aggarwal et al., "Enhanced production of multi-strange hadrons in high-multiplicity proton-proton collisions," *Nature Physics*, vol. 13, no. 6, pp. 535–539, 2017.

[11] R. L. Jaffe, "Exotica," *Physics Reports*, vol. 409, no. 1, pp. 1–45, 2005.

[12] C. Tsallis, "Possible generalization of Boltzmann-Gibbs statistics," *Journal of Statistical Physics*, vol. 52, no. 1-2, pp. 479–487, 1988.

[13] J. Cleymans and M. W. Paradza, "Tsallis statistics in high energy physics: chemical and thermal freeze-outs," *Physics*, vol. 2, no. 4, pp. 654–664, 2020.

[14] H. Zheng and L. L. Zhu, "Can Tsallis distribution fit all the particle spectra produced at RHIC and LHC?," *Advances in High Energy Physics*, vol. 2015, Article ID 180491, 9 pages, 2015.

[15] T. S. Biró, G. Purcsel, and K. Ürmössy, "Non-extensive approach to quark matter," *The European Physical Journal A*, vol. 40, no. 3, pp. 325–340, 2009.

[16] H. Zheng, L. L. Zhu, and A. Bonasera, "Systematic analysis of hadron spectra in p+p collisions using Tsallis distributions," *Physical Review D*, vol. 92, no. 7, article 074009, 2015.

[17] S. Chatrchyan, V. Khachatryan, A. M. Sirunyan et al., "Study of the inclusive production of charged pions, kaons, and protons in pp collisions at $\sqrt{s} = 0.9$, 2.76, and 7 TeV," *The European Physical Journal C*, vol. 72, no. 10, article 2164, 2012.

[18] B. I. Abelev, M. M. Aggarwal, Z. Ahammed et al., "Enhanced strange baryon production in Au+Au collisions compared to p+p at $\sqrt{s_{NN}} = 200$ GeV," *Physical Review C*, vol. 77, no. 4, article 044908, 2008.

[19] S. V. Afanasiev, T. Anticic, D. Barna et al., "Ξ^- and $\bar{\Xi}^+$ production in central Pb+Pb collisions at 158 GeV/c per nucleon," *Physics Letters B*, vol. 538, no. 3–4, pp. 275–281, 2002.

[20] E. Andersen, F. Antinori, N. Armenise et al., "Strangeness enhancement at mid-rapidity in Pb-Pb collisions at 158A GeV/c," *Physics Letters B*, vol. 449, no. 3–4, pp. 401–406, 1999.

[21] F. Antinori, P. A. Bacon, A. Badalà et al., "Energy dependence of hyperon production in nucleus-nucleus collisions at SPS," *Physics Letters B*, vol. 595, no. 1–4, pp. 68–74, 2004.

[22] P.-P. Yang, F.-H. Liu, and R. Sahoo, "A new description of transverse momentum spectra of identified particles produced in proton-proton collisions at high energies," *Advances in High Energy Physics*, vol. 2020, Article ID 6742578, 9 pages, 2020.

[23] Y.-M. Tai, P.-P. Yang, and F.-H. Liu, "An analysis of transverse momentum spectra of various jets produced in high energy collisions," *Advances in High Energy Physics*, vol. 2021, Article ID 8832892, 16 pages, 2021.

[24] X.-H. Zhang, Y.-Q. Gao, F.-H. Liu, and K. K. Olimov, "Thermal freeze-out parameters and pseudoentropy from charged hadron spectra in high-energy collisions," *Advances in High Energy Physics*, vol. 2022, Article ID 7499093, 36 pages, 2022.

[25] C. P. Robert and G. Casella, *Monte Carlo Statistical Methods*, Springer Press, New York, 2nd edition, 2004.

[26] N. Metropolis and S. Ulam, "The Monte Carlo method," *Journal of the American Statistical Association*, vol. 44, no. 247, pp. 335–341, 1949.

[27] D. E. Raeside, "Monte Carlo principles and applications," *Physics in Medicine & Biology*, vol. 21, no. 2, pp. 181–197, 1976.

[28] G. Wilk and Z. Włodarczyk, "Consequences of temperature fluctuations in observables measured in high-energy collisions," *The European Physical Journal A*, vol. 48, no. 11, article 161, 2012.

[29] T. S. Biró, G. G. Barnaföldi, G. Biró, and K. M. Shen, "Near and far from equilibrium power-law statistics," *Journal of Physics: Conference Series*, vol. 779, article 012081, 2017.

[30] G. Wilk and Z. Włodarczyk, "Interpretation of nonextensivity parameter q in some applications of Tsallis statistics and Lévy distributions," *Physical Review Letters*, vol. 84, no. 13, pp. 2770–2773, 2000.

[31] T. S. Biró, P. Ván, G. G. Barnaföldi, and K. Ürmössy, "Statistical power law due to reservoir fluctuations and the universal thermostat independence principle," *Entropy*, vol. 16, no. 12, pp. 6497–6514, 2014.

[32] E. Schnedermann, J. Sollfrank, and U. Heinz, "Thermal phenomenology of hadrons from 200A GeV S+S collisions," *Physical Review C*, vol. 48, no. 5, pp. 2462–2475, 1993.

[33] M. Waqas and B.-C. Li, "Kinetic freeze-out temperature and transverse flow velocity in Au-Au collisions at RHIC-BES energies," *Advances in High Energy Physics*, vol. 2020, Article ID 1787183, 14 pages, 2020.

[34] P. K. Khandai, P. Sett, P. Shukla, and V. Singh, "System size dependence of hadron p_T spectra in $p+p$ and Au+Au collisions at $\sqrt{s_{NN}} = 200$ GeV," *Journal of Physics G: Nuclear and Particle Physics*, vol. 41, no. 2, article 025105, 2014.

[35] K. K. Olimov, S. Z. Kanokova, K. Olimov et al., "Average transverse expansion velocities and global freeze-out temperatures in central Cu+Cu, Au-Au, and Pb+Pb collisions at high energies at RHIC and LHC," *Modern Physics Letters A*, vol. 35, no. 14, article 2050115, 2020.

[36] K. K. Olimov, S. Z. Kanokova, A. K. Olimov et al., "Combined analysis of midrapidity transverse momentum spectra of the charged pions and kaons, protons and antiprotons in $p+p$ and Pb+Pb collisions at $(s_{nn})^{1/2} = 2.76$ and 5.02 TeV at the LHC," *Modern Physics Letters A*, vol. 35, no. 29, article 2050237, 2020.

[37] K. K. Olimov, A. Iqbal, and S. Masood, "Systematic analysis of midrapidity transverse momentum spectra of identified charged particles in $p+p$ collisions at $(s_{nn})^{1/2} = 2.76$, 5.02, and 7 TeV at the LHC," *International Journal of Modern Physics A*, vol. 35, no. 27, article 2050167, 2020.

[38] Z.-J. Xiao and C.-D. Lü, *Introduction to Particle Physics*, Science Press, Beijing, China, 2016.

[39] B. Abelev, J. Adam, D. Adamová et al., "$K^*(892)^0$ and $\phi(1020)$ production in Pb-Pb collisions at $\sqrt{s_{NN}} = 2.76$ TeV," *Physical Review C*, vol. 91, no. 2, article 024609, 2015.

[40] B. Abelev, J. Adam, D. Adamova et al., "K^0_S and Λ production in Pb-Pb collisions at $\sqrt{s_{NN}} = 2.76$ TeV," *Physical Review Letters*, vol. 111, no. 22, article 222301, 2013.

[41] B. Abelev, J. Adam, D. Adamová et al., "Multi-srtange baryon production at mid-rapidity in Pb-Pb collisions at $\sqrt{s_{NN}} = 2.76$ TeV," *Physics Letters B*, vol. 728, pp. 216–227, 2014.

[42] S. Acharya, D. Adamová, S. P. Adhya et al., "Production of charged pions, kaons and (anti-)protons in Pb-Pb and inelastic pp collisions at $\sqrt{s_{NN}} = 5.02$ TeV," *Physical Review C*, vol. 101, no. 4, article 044907, 2020.

[43] S. Acharya, D. Adamová, A. Adler et al., "Evidence of rescattering effect in Pb-Pb collisions at the LHC through production of $K^*(892)^0$ and $\phi(1020)$ mesons," *Physics Letters B*, vol. 802, article 135225, 2020.

[44] J. Adam, D. Adamová, M. M. Aggarwal, and ALICE Collaboration, "Production of $K^*(892)^0$ and $\phi(1020)$ in p-Pb collisions at $\sqrt{s_{NN}} = 5.02$ TeV," *The European Physical Journal C*, vol. 76, no. 5, article 245, 2016.

[45] B. Abelev, J. Adam, D. Adamová et al., "Multiplicity dependence of pion, kaon, proton and lambda production in p-Pb collisions at $\sqrt{s_{NN}} = 5.02$ TeV," *Physics Letters B*, vol. 728, pp. 25–38, 2014.

[46] S. Acharya, D. Adamova, A. Adler et al., "Production of pions, kaons, (anti-)protons and ϕ mesons in Xe-Xe collisions at $\sqrt{s_{\mathrm{NN}}} = 5.44$ TeV," *The European Physical Journal C*, vol. 81, no. 7, article 584, 2021.

[47] V. Andreev, A. Baghdasaryan, A. Baty et al., "Measurement of charged particle multiplicity distributions in DIS at HERA and its implication to entanglement entropy of partons," *The European Physical Journal C*, vol. 81, no. 3, article 212, 2021.

[48] X. Feal, C. Pajares, and R. A. Vazquez, "Thermal behavior and entanglement in Pb-Pb and p−p collisions," *Physical Review C*, vol. 99, no. 1, article 015205, 2019.

[49] Z. Tu, D. E. Kharzeev, and T. Ullrich, "Einstein-Podolsky-Rosen paradox and quantum entanglement at subnucleonic scales," *Physical Review Letters*, vol. 124, no. 6, article 062001, 2020.

[50] E. Schnedermann and U. Heinz, "Circumstantial evidence for transverse flow in 200A GeV S+S collisions," *Physical Review Letters*, vol. 69, no. 20, pp. 2908–2911, 1992.

[51] B. I. Abelev, M. M. Aggarwal, Z. Ahammed et al., "Systematic measurements of identified particle spectra in pp, d+Au, and

Au+Au collisions at the STAR detector," *Physical Review C*, vol. 79, no. 3, article 034909, 2009.

[52] B. I. Abelev, M. M. Aggarwal, Z. Ahammed et al., "Identified particle production, azimuthal anisotropy, and interferometry measurements in Au+Au collisions at $\sqrt{s_{NN}}$ = 9.2 GeV," *Physical Review C*, vol. 81, no. 2, article 024911, 2010.

[53] M. Waqas, B.-X. Peng, F. -H. Liu, M. Ajaz, and A. A. K. H. Ismail, "Investigation of the freeze-out parameters in B-B, O-O, Ca-Ca and Au-Au collisions at 39 GeV," *The European Physical Journal Plus*, vol. 137, article 1026, 2022.

[54] E. K. G. Sarkisyan and A. S. Sakharov, "Multihadron production features in different reactions," *AIP Conference Proceedings*, vol. 828, pp. 35–41, 2006.

[55] E. K. G. Sarkisyan and A. S. Sakharov, "Relating multihadron production in hadronic and nuclear collisions," *The European Physical Journal C*, vol. 70, no. 3, pp. 533–541, 2010.

[56] A. N. Mishra, R. Sahoo, E. K. G. Sarkisyan, and A. S. Sakharov, "Effective-energy budget in multiparticle production in nuclear collisions," *The European Physical Journal C*, vol. 74, no. 11, article 3147, 2014.

[57] E. K. G. Sarkisyan, A. N. Mishra, R. Sahoo, and A. S. Sakharov, "Multihadron production dynamics exploring the energy balance in hadronic and nuclear collisions," *Physical Review D*, vol. 93, no. 5, article 054046, 2016.

[58] E. K. G. Sarkisyan, A. N. Mishra, R. Sahoo, and A. S. Sakharov, "Centrality dependence of midrapidity density from GeV to TeV heavy-ion collisions in the effective-energy universality picture of hadroproduction," *Physical Review D*, vol. 94, no. 1, article 011501(R), 2016.

[59] E. K. G. Sarkisyan, A. N. Mishra, R. Sahoo, and A. S. Sakharov, "Effective-energy universality approach describing total multiplicity centrality dependence in heavy-ion collisions," *EPL (Europhysics Letters)*, vol. 127, article 62001, 2019.

[60] A. N. Mishra, A. Ortiz, and G. Paic, "Intriguing similarities of high-p_T particle production between *pp* and *A-A* collisions," *Physical Review C*, vol. 99, no. 3, article 034911, 2019.

[61] P. Castorina, A. Iorio, D. Lanteri, H. Satz, and M. Spousta, "Universality in hadronic and nuclear collisions at high energy," *Physical Review C*, vol. 101, no. 5, p. article 054902, 2020.

[62] E. L. Bratkovskaya, M. Bleicher, C. Greiner et al., "Collective flow signals the quark gluon plasma," *AIP Conference Proceedings*, vol. 739, pp. 305–329, 2004.

[63] K. G. Zloshchastive, "Singular shells of quark-gluon matter," *International Journal of Modern Physics D*, vol. 8, no. 3, pp. 363–371, 1999.

[64] A. K. Chaudhuri and U. Heinz, "Effect of jet quenching on hydrodynamical evolution of QGP," *Journal of Physics G*, vol. 34, no. 8, pp. S689–S692, 2007.

[65] T. Niida and Y. Miake, "Signatures of QGP at RHIC and the LHC," *AAPPS Bulletin*, vol. 31, no. 1, article 12, 2021.

[66] C. Gale, Y. Hidaka, S. Jeon et al., "Production and elliptic flow of dileptons and photons in a matrix model of the quark-gluon plasma," *Physical Review Letters*, vol. 114, no. 7, article 072301, 2015.

[67] H. Stöcker, "Collective flow signals the quark-gluon plasma," *Nuclear Physics A*, vol. 750, no. 1, pp. 121–147, 2005.

[68] X.-H. Zhang, F.-H. Liu, K. K. Olimov, and A. Deppman, "Random statistical analysis of transverse momentum spectra of strange particles and dependence of related parameters on centrality in high energy collisions at the LHC," 2022, https://arxiv.org/abs/2209.03894.